Additive Manufacturing 47 (2021) 102292

Contents lists available at ScienceDirect

Additive Manufacturing

journal homepage: www.elsevier.com/locate/addma

Research Paper

Structural integrity of additively manufactured aluminum alloys: Effects of build orientation on microstructure, porosity, and fatigue behavior

P.D. Nezhadfar [a,b], Spencer Thompson [c], Ankit Saharan [c], Nam Phan [d], Nima Shamsaei [a,b,*]

[a] Department of Mechanical Engineering, Auburn University, Auburn, AL 36849, USA
[b] National Center for Additive Manufacturing Excellence (NCAME), Auburn University, Auburn, AL 36849, USA
[c] EOS North America, 3813 Helios Way #B298, Pflugerville, TX 78660, USA
[d] Structures Division, US Naval Air Systems Command (NAVAIR), Patuxent River, MD 20670, USA

ARTICLE INFO

Keywords:
Laser beam powder bed fusion (LB-PBF/L-PBF)
Aluminum alloys
Fatigue behavior
Microstructure
Porosity

ABSTRACT

The use of aluminum (Al) alloys for additive manufacturing (AM) has recently gained significant attention, specifically in the aerospace industry. This has been resulting in introducing new high strength Al alloys that are more compatible with the AM processes. However, it is critical to investigate the structural integrity of these newly developed Al alloys prior to being deployed in safety-critical load-bearing applications. This study investigates and compares the microstructure, porosity, and fatigue behavior of five different contemporary Al alloys fabricated via a laser beam powder bed fusion (LB-PBF) AM process. Vertically and horizontally built specimens out of AlSi10Mg, Scalmalloy, QuesTek Al, AD1, and AlF357 are fabricated to capture any effects of build orientation on the structural integrity of these alloys. Despite the variation in micro-/defect-structure of vertical and horizontal specimens, no significant build orientation dependency is observed on fatigue behavior of AlSi10Mg, Scalmalloy, and AD1 alloys. However, AlF357 and QuesTek Al show some anisotropic behavior in the high cycle fatigue regime. Among the LB-PBF Al alloys investigated, Scalmalloy and AD1 are found to have the highest fatigue resistance ascribed to their superfine microstructure.

1. Introduction

Additive manufacturing (AM) is rapidly becoming a strategic technology generating revenues in various industries such as defense, aerospace, automotive, and biomedical. These industries can derive value from the profound benefits of AM, such as the manufacture of near-net-shape parts with complex geometries, reduction in lead times, reduction of component weight due to freedom in design, potential cost reductions, and environmentally friendly production. Along with various advantages, there are also many challenges associated with the AM techniques [1]. The unique thermal history of the AM processes (i.e., high cooling/solidification rate, thermal gradient, etc.) typically induces residual stresses, microstructural anisotropy, surface roughness and leads to the formation of volumetric defects (e.g., pores and lack of fusions (LoFs)) [2,3].

Although the influence of defects (e.g., surface roughness, pore, and LoF) may be minimal on the static properties, these flaws can deteriorate the fatigue performance of additively manufactured (AM) parts significantly [4]. Recent studies [5,6] reported that the defects are the source of scatter in fatigue results of AM metallic materials. The detrimental effect of process-induced defects (i.e., pore, LoF) is not limited to the room temperature fatigue behavior of AM materials. Bao et al. [7,8] reported that the pores and LoF defects can elongate during cyclic deformation at elevated temperatures and result in fatigue failure by microvoid formation.

Many studies have been conducted to investigate the fatigue behavior of various AM metallic materials; a great deal of these works has been focused on titanium alloys [9–11], stainless steels [12–14], and Ni-super alloys [15–17]. Recently, Aluminum (Al) alloys have drawn much attention for fabricating parts via AM processes. Al alloys are known for their high strength-to-weight ratio, adequate hardenability,

Abbreviations: Al, aluminum; AM, additive manufacturing/additively manufactured; AMSC, additive manufacturing standardization collaborative; BCC, body-centered cube; BSD, Backscatter diffraction; EBSD, electron backscatter diffraction; FCC, face-centered cube; H, horizontal; HCF, high cycle fatigue; HIP, hot isostatic pressing; IPF, inverse pole figure; LoF, lack of fusion; LB-PBF/L-PBF, laser beam powder bed fusion/fused; NHT, non-heat treated; SEM, scanning electron microscope/microscopy; SS, stainless steel; TD, transverse direction; V, vertical; VHCF, very high cycle fatigue.

* Corresponding author at: Department of Mechanical Engineering, Auburn University, Auburn, AL 36849, USA.
E-mail address: shamsaei@auburn.edu (N. Shamsaei).

https://doi.org/10.1016/j.addma.2021.102292
Received 2 July 2021; Received in revised form 25 August 2021; Accepted 5 September 2021
Available online 10 September 2021

Nomenclature

$2N_f$	reversals to failure
R_ε	ratio of minimum strain to the maximum strain
%El	percent elongation to failure
ε_a	strain amplitude
ε_{max}	maximum strain
ε_{min}	minimum strain
σ_a	stress amplitude
σ_m	mean stress
σ_y	yield strength
σ_U	ultimate tensile strength

good corrosion resistance, and excellent weldability, making them suitable for being deployed in a wide range of applications, specifically in the aerospace industry [18,19]. However, as compared to other materials, AM of Al alloys is even more challenging; Al powder particles are inherently light, have poor flowability, attract moisture due to the hydrophilic nature of Al, and have high thermal conductivity [18]. In addition, Al powder particles are highly susceptible to oxidation, and their low melt viscosity promotes porosity formation [20]. Such issues in the manufacture of Al alloys may induce defects in the parts, consequently influencing their mechanical properties, especially their fatigue performance.

Al-Si cast alloys (e.g., AlSi10Mg) are typically easier to process by AM as compared to the wrought Al alloys (e.g., AA6061 [21], A7075 [22]). There are quite a few papers in the literature that present various parameters influencing the fatigue performance of AM AlSi10Mg [23–27]. Jian et al. [28] studied the effect of powder particle size on the high cycle fatigue (HCF) and very high cycle fatigue (VHCF) behavior of laser beam powder bed fused (LB-PBF) AlSi10Mg. They showed that using smaller powder particles reduces the porosity, and consequently, enhances the fatigue strength of LB-PBF AlSi10Mg in non-heat treated (NHT) condition. Wu et al. [6] investigated the effect of volumetric defect size and population, as well as the orientation of LoF defects with respect to the loading direction, on the fatigue anisotropy behavior of LB-PBF AlSi10Mg. Lower ductility and fatigue strength were reported when the loading direction was parallel to the build direction as compared to the case where the loading direction was perpendicular to the build direction. This was attributed to size of the projected area of LoF defects on the plane perpendicular to the loading direction, which was larger when the loading direction was parallel to the build direction.

Maskery et al. [25] studied the effect of heat treatment and reported that performing T6 heat treatment (i.e., a solution treatment for 1 h at 520 °C, water quenched, followed by aging for 6 h at 160 °C, air-cooled) enhances the ductility as well as fatigue resistance of LB-PBF AlSi10Mg. In addition, Ngnekou et al. [29] found that while a T6-type heat treatment (i.e., a solution treatment for 8 h at 540 °C, followed by aging for 10 h at 160 °C, air-cooled) enhances the fatigue resistance of the material, it may result in build orientation dependency in fatigue performance of LB-PBF AlSi10Mg. This has been associated with the defect characteristics (i.e., size, shape, frequency, etc.) in different build orientations and the increased material sensitivity to the presence of defects after applying T6-type heat treatment. The EOS datasheet for the LB-PBF AlSi10Mg suggests that T6-type heat treatment may not be the best option for this material [30]. The traditional T6 heat treatment is proven to be challenging for certain sand-casting Al alloys (e.g., AlSi7Mg0.6) due to the possibility of blistering hydrogen porosity formation [31]. Therefore, EOS recommends only stress relieving instead of T6 heat treatment [30].

There are also limited studies on the fatigue behavior of AM AlSi7Mg in the literature; Lesperance et al. [32] investigated the VHCF behavior of LB-PBF AlSi7Mg using ultrasonic testing, and compared the results with those of the cast A356 alloy, and reported similar VHCF behaviors. Another AM Al alloy is A357, which is the modified version of A356 alloy with higher strength; although there are several studies on process optimization and microstructure characterization of LB-PBF A357, there are not many studies on the fatigue performance of this alloy in the literature. In one study, Bassoli et al. [33] investigated the fatigue behavior of LB-PBF AlA357 in NHT condition and reported somewhat similar fatigue behavior to LB-PBF AlSi10Mg alloy. Recently, AlF357 alloy, beryllium free derivative of the AlA357 alloy, has also been introduced to AM community [34]. However, there is no fatigue data available for this alloy in the literature, and it will be investigated in the present study.

Scalmalloy, introduced by the Airbus APWorks, is one of the recently developed Al alloys for AM [35]. This alloy possesses high yield and ultimate tensile strengths combined with acceptable ductility due to its unique microstructure comprised of nano-size grains and nano-size $Al_3(Sc,Zr)$ precipitates [36]. There are only a few studies on the fatigue behavior of Scalmalloy in the literature which show superior fatigue performance of LB-PBF Scalmalloy to that of LB-PBF AlSi10Mg [37]. Muhammad et al. [38] recently compared the fatigue performance of LB-PBF AlSi10Mg, Scalmalloy, and a new Al alloy developed by QuesTek Innovations LLC. They reported higher fatigue resistance for Scalmalloy as compared to other Al alloys, which was attributed to its higher toughness (i.e., high tensile strength and ductility) ascribed to its unique nano-size microstructure.

Considering the ongoing alloy development for AM, especially the Al alloys with different microstructural features (i.e., grain morphology and size, precipitates, etc.), it is crucial to study their fatigue performance to fill the Gap FMP1 on “materials properties” according to the AM standardization road map compiled by America Makes & ANSI additive manufacturing standardization collaborative (AMSC) [39]. In line with this goal, the current study aims to investigate the potential anisotropy in fatigue performance of some contemporary LB-PBF Al alloys and correlate them with their micro-/defect-structure (i.e., microstructure and the defect structure in micro scale). These alloys with different microstructural characteristics (i.e., grain structure, precipitates, etc.), and often better tensile strength, may or may not possess better fatigue behavior due to the presence of volumetric defects. In addition, it has been shown that the thermal history experienced by the parts is varied in different build orientations, which may result in anisotropy in the mechanical behavior as a result of variation in defect type, size, and population [6,40]. Therefore, generating data and evaluating the fatigue behavior of the LB-PBF Al specimens fabricated in different build orientations seems necessary.

This article is organized in the following order: in Section 2, the materials and methods are presented in detail. In Section 3, the experimental results, including the micro-/defect-structure analysis, and fatigue data, are presented. In Section 4, the fatigue behavior of the LB-PBF Al alloys is discussed and correlated to their micro-/defect-structure. Finally, some conclusions are drawn based on the experimental observations in this study and listed in Section 5.

2. Materials and methods

2.1. Al alloys

In this study, five different pre-alloyed gas atomized Al powders were used to fabricate the specimens; the chemical composition, powder particle size range, and the powder manufacturer for each of these alloys are listed in Table 1, and the scanning electron microscopy (SEM) images of the powder particles are shown in Fig. 1. However, the detailed chemical composition for AD1 is not listed for the sake of confidentiality; the AD1 is a newly developed Al-Mg-Zr alloy possessing a high strength after heat treatment. AlF357 is a ‘Be’ free derivative of AlA357 and AlA356 developed to avoid environmental and health risks with slight reduction in strength as compared to the AlA357 alloy [34]. The

Table 1
The chemical composition of Al powders used in this study reported by the corresponding powder manufacturer.

Alloy Element	AlSi10Mg	Scalmalloy	QuesTek Al	AD1	AlF357
Al	Bal.	Bal.	Bal.	Al-Mg-Zr alloy	Bal.
Si	9–11	0.20	2.37		6.5–7.5
Fe	< 0.55	0.10	0.035		0.1 max
Cu	< 0.05	–	–		0.2 max
Mn	< 0.45	0.50	0.35		0.1
Mg	0.2–0.45	4.60	6.79		0.4–0.7
Ni	< 0.05	–	–		–
Zn	< 0.10	–	–		0.1 max
Pb	< 0.05	–	–		–
Sn	< 0.05	–	–		–
Ti	< 0.15	–	–		0.04–0.2
O	–	0.04	–		–
Sc	–	0.70	–		–
Zr	–	0.30	–		–
Be	–	–	–		< 0.002
Minimum Particle Size	20 μm	20 μm	20 μm	15 μm	20 μm
Maximum Particle Size	63 μm	63 μm	63 μm	45 μm	90 μm
Powder Manufacturer	EOS	Carpenter Additive®	Connecticut Engineering Associates Corporation (CEAC)	EOS	EOS

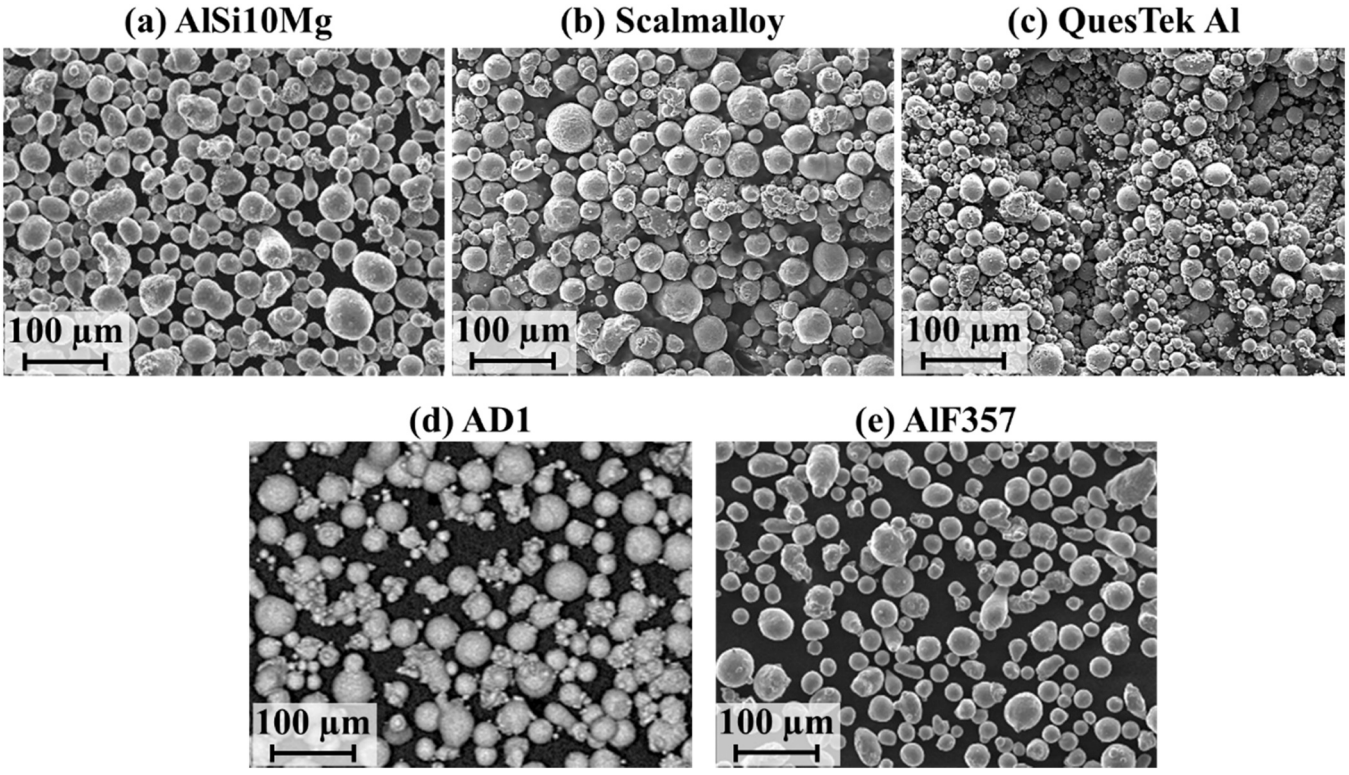

Fig. 1. The SEM images of the LB-PBF Al powder particles: (a) AlSi10Mg, (b) Scalmalloy, (c) QuesTek Al, (d) AD1, and (e) AlF357.

QuesTek Al has been reported to be a high strength, highly corrosion-resistant, and low-cost alloy (as it contains no expensive alloying elements) [38].

2.2. Specimens Fabrication

Specimens were fabricated via the LB-PBF process, EOS M290, under argon shielding gas. It must be mentioned that EOS recommended process parameters were used for AlSi10Mg, AD1, and AlF357 alloys, while the process parameters used for fabrication of Scalmalloy and QuesTek Al were not necessarily the most optimized ones. The process parameters used for Scalmalloy were adapted from [41], and the ones for the QuesTek Al were suggested by QuesTek Innovations LLC. for EOS M280, as listed in Table 2. It must be noted that the detailed default EOS process parameters for other alloys are not provided for the sake of confidentiality. However, similar strip scan strategy was used for all the alloys.

Table 2
LB-PBF process parameters for each of the Al alloys investigated in this study.

Alloy	Laser power (W)	Laser scan speed (mm/s)	Hatching distance (mm)	Layer thickness (mm)
Scalmalloy [41]	370	1000	0.10	0.03
QuesTek Al	370	1040	0.17	0.03

Cylindrical rods with 12 mm diameter and 90 mm length were fabricated in both vertical (V) and horizontal (H) orientations. The

vertical specimens were directly deposited to the build plate, while the horizontal ones were fabricated on top of support structures. The build layout, as well as the powder spread and argon flow directions are shown in Fig. 2(a). All the specimens were heat treated after fabrication using the procedure recommended for each alloy listed in Table 3. According to the manufacturer datasheets, the heat treatment procedure for the LB-PBF AlSi10Mg was adopted from [42] and AlF357 from [34], reported as the optimal heat treatments for these alloys. The QuesTek Innovations LLC. and EOS suggested the heat treatment procedures for the LB-PBF QuesTek Al and AD1, respectively. For the Scalmalloy, the applied heat treatment procedure has been reported as the optimal heat treatment for this alloy resulting into the highest tensile strength along with acceptable ductility [36]. Tensile properties of the heat treated LB-PBF Al alloys are adopted from the literature in both build orientations (i.e., vertical and horizontal) and listed in Table 4.

The heat treatment temperatures applied for the LB-PBF AlSi10Mg, Scalmalloy, and QuesTek Al are all below their solutionizing temperature (i.e., 450–575 °C). However, the AlF357 alloy was undergone T6 two-stage heat treatment comprising solutionizing and aging procedures. The heat treatments were applied prior to removing the specimens off the build plate to avoid distortion during cutting due to the residual stresses. A thermocouple-controlled box furnace was employed to perform the heat treatments under Ar atmosphere, with the build plates heated up from room temperature to the target temperature to avoid oxidations. The specimens were cut off the build plate after heat treatment and further machined to the final geometry of the cylindrical specimens with a uniform gage section for fatigue testing following ASTM E606 [43], shown in Fig. 2(b).

Table 3
Heat treatment procedures employed for the post process thermal treatment of the LB-PBF Al specimens. The heat treatment procedures for AlSi10Mg, Scalmalloy, and QuesTek Al alloys are adopted from [38], for AlF357 from [34], and EOS suggested the heat treatment procedure for AD1.

Alloy	Temperature (°C)	Duration (hour)	Quenching Environment
AlSi10Mg	270	1.5	Furnace
Scalmalloy	325	4	Furnace
QuesTek Al	185	2	Air
AD1	400	6	Air
AlF357	540	0.5	Water
	165	6	Air

Table 4
Tensile properties of LB-PBF Al alloys adopted from literature and undergone the same heat treatment procedures listed in Table 3. Note that the properties for the AD1 have been provided by EOS.

Alloy	Build Orientation	σ_y (MPa)	σ_U (MPa)	%El
AlSi10Mg[42]	Vertical	225	350	9.0
	Horizontal	220	340	12.0
Scalmalloy[38,44]	Vertical	508	530	16.0
	Horizontal	520	531	14.0
QuesTek Al[38]	Vertical	421	496	5.0
	Horizontal	NA	NA	NA
AD1	Vertical	409	435	18.0
	Horizontal	419	439	19.0
AlF357[34]	Vertical	250	390	11.5
	Horizontal	255	370	11.5

2.3. Micro-/defect-structure characterization

The microstructure characterization of the LB-PBF Al alloys was performed on the planes parallel and perpendicular to the build direction via electron backscatter diffraction (EBSD) analysis. The specimens were cut, ground and polished prior to performing EBSD analysis. A Zeiss 550 Crossbeam FIB/SEM with an Oxford EBSD detector was used for conducting the EBSD analysis. The scans were performed with a 1 μm step size at the 200X magnification, and the AzTec Crystal software by Oxford was used for post processing the data. The X-ray CT scans were conducted using a Zeiss Xradia 620 system to visualize the volumetric defects within the fabricated parts. The scans were performed on a 6.5-mm length in the middle of the gage section of the machined fatigue specimens.

2.4. Fatigue testing and fractography

Uniaxial fully-reversed ($R_\varepsilon = \varepsilon_{min}/\varepsilon_{max} = -1$) strain-controlled fatigue tests were performed based on ASTM E606 standard [43] using an MTS landmark servohydraulic testing machine with 100 kN load cells. Fatigue tests were carried out for two different strain amplitude levels of 0.002 mm/mm and 0.003 mm/mm. To control the tests and measure the strain at the gage section, an MTS mechanical extensometer was attached to the gage section on two locations coated by acrylic to avoid any slippage and scratches by the extensometer's blades. To ensure the certainty of the results, three tests were conducted at each strain amplitude level per material. In order to investigate the failure mechanisms, fractography analyses were conducted on the fracture surfaces of selected specimens. The fracture surfaces were sonicated and cleaned

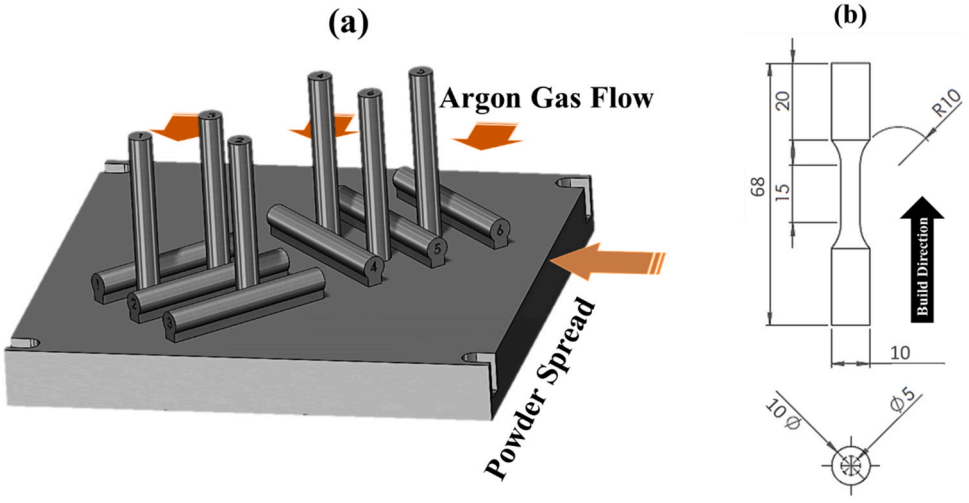

Fig. 2. (a) The build layout, and (b) drawing of the final geometry after machining for the fatigue specimens following ASTM E606 (note that the dimensions are in 'mm' and the build orientation shown is corresponding to a vertical specimen).

prior to performing the fractography.

3. Experimental results

In this section, the experimental observations on the micro-/defect-structure and fatigue behavior of investigated LB-PBF Al alloys are presented. The fatigue failure mechanisms of these alloys are also examined through fractography analysis. Further discussions on the structure-property relationships of these Al alloys are included in Section 4.

3.1. Microstructure of LB-PBF Al alloys

The microstructure characterization results of the heat treated vertical and horizontal LB-PBF Al specimens are presented in Fig. 3. The schematic in this figure shows the planes on which the microstructure is characterized for vertical and horizontal specimens. The XYZ-coordinate presented here is based on the one recommended in [45]; the build direction is also shown by a black arrow parallel to the Z-axis. The inverse pole figure (IPF) maps are shown both on XY-plane (i.e., perpendicular to the build direction) and XZ-plane (i.e., parallel to the build direction). The microstructure is shown on both XY- and XZ-planes for the vertical specimens, while it is only shown on XZ-plane for the horizontal specimens; the exact XY-plane (i.e., perpendicular to the build direction) for the horizontal specimens were not easy to find after removing the specimens off the build platform because of the circular cross-section. The IPF sets parallel to X, Y, and Z-axis are shown underneath the corresponding maps to capture the crystallographic orientation of the grains along different directions.

The loading directions are also shown in the schematics for different build orientations. It must be noted that the loading direction for the vertical specimens is parallel to the Z-axis (i.e., parallel to the crystallographic orientation of grains shown by the IPF map), while it is parallel to the Y-axis (i.e., perpendicular to the crystallographic orientation of grains shown in the IPF map) for the horizontal specimens. Therefore, to correlate the loading direction with the crystallographic orientation of the grains, the IPF parallel to the Z-axis for the vertical specimens and the IPF parallel to the Y-axis for the horizontal specimens should be analyzed.

3.1.1. Grain structure

The typical grain structure induced by the AM process, i.e., the columnar grains, and equiaxed grains mostly surrounding the melt pool boundaries, are observed for all the LB-PBF Al alloys even after performing heat treatment (see Fig. 3). The grain structure for the vertical and horizontal LB-PBF Al specimens on XZ-plane (i.e., parallel to the build direction) are found to be very similar. Likewise, the grain structure on the XY-plane (see the first column in Fig. 3) is expected to be similar in vertical and horizontal specimens, comprising an equiaxed view of the columnar grains seen on the XZ-plane. The LB-PBF AlSi10Mg (see Fig. 3(a)) has a similar grain structure to the ones for the QuesTek Al (see Fig. 3(c)) and AlF357 (see Fig. 3(e)) alloys, which includes primarily elongated columnar grains along with equiaxed grains around the melt pool boundaries on XZ-plane and equiaxed grains on XY-plane.

It can be seen that Scalmalloy (Fig. 3(b)) and AD1 (Fig. 3(d)) have a super fine grain structure comprising ultrafine/nano-size equiaxed grains as well as more refined columnar grains compared to the other alloys. The equiaxed grains in the microstructure of LB-PBF AD1 alloy (Fig. 3(d)), however, are not limited to the regions around the melt pool boundaries, which is the case for Scalmalloy. In addition, the columnar grains in AD1 seem to be finer than those of Scalmalloy. This may be due to the differences in the chemical composition of Scalmalloy and AD1, as well as the process parameters used for fabrication of these alloys. It is worth noting that the black regions in the Scalmalloy and AD1 microstructures (Fig. 3(b) and (d), respectively) are attributed to the regions surrounding the melt pools with nano-size grains, which could not be characterized with the step size used for the EBSD scans. The ultrafine/nano-size equiaxed grains in LB-PBF Scalmalloy and AD1 (Al-Mg-Zr alloy) are formed due to the presence of coherent nano-size Al_3Sc and Al_3Zr precipitates, which serve as grain growth inhibitors as well as heterogeneous grain nucleation sites [46,47].

The grain size analysis was conducted using EBSD and the results are shown in Fig. 4. It can be seen that there is no difference in grain size between the vertical and horizontal specimens (the standard deviation error bars are also overlapped). The LB-PBF Scalmalloy and AD1 specimens possess almost identical average grain size (note that the nano-size grains, the black regions in IPF maps in Fig. 3, are not included), which is finer compared to other alloys. The LB-PBF AlSi10Mg, QuesTek Al, and AlF357 have almost similar grain sizes.

3.1.2. Crystallographic orientation of the grains

In general, the $< 001 >$ is the preferred grain growth direction in cubic structure materials (i.e., face-centered cube (FCC) and body-centered cube (BCC)), and one of the well-known crystallographic grain orientations for most of the AM materials in non-heat treated (NHT) condition. This is mainly due to the high cooling rate and conduction heat transfer toward the build platform leading to epitaxial grain growth [48]. The crystallographic orientation of the grains for the LB-PBF Al alloys, parallel to the build direction, can be observed from the IPF //Z-axis in Fig. 3. It can be seen that AlSi10Mg (both vertical and horizontal in Fig. 3(a)) and Scalmalloy (both vertical and horizontal in Fig. 3(b)) have $< 001 >$ preferred crystallographic grain orientation, while the grains in QuesTek Al (both vertical and horizontal in Fig. 3(c)) and AD1 (both vertical and horizontal in Fig. 3(d)) are almost randomly oriented. For the AlF357 alloy (Fig. 3(e)), the vertical specimen has mostly $< 001 >$-oriented grains, while the horizontal specimen has almost randomly oriented grains with weaker texture (i.e., 2.57 intensity in the vertical specimen compared to 1.8 in the horizontal specimen).

It must be noted that the heat treatments applied on AlSi10Mg, Scalmalloy, QuesTek Al, and AD1 were below the solutionizing temperature, considered as stress-relief heat treatments, which are not expected to change the crystallographic texture of the grains. Therefore, the crystallographic orientation of the grains is still inherited from the fabrication process. However, it has been reported that the high heat input, in other words, lower cooling/solidification rate, may alter the crystallographic orientation of the grains during fabrication [14]. For the AlF357 alloy, however, the crystallographic orientation of the grains and the texture intensity may have been affected by the heat treatment procedure applied (i.e., solutionizing followed by aging).

3.2. Defect-structure of LB-PBF Al alloys

The X-ray CT scan results from a 6.5-mm length X 5-mm diameter volume in the gage section of vertical and horizontal LB-PBF Al specimens and defect density (i.e., the accumulative %volume of defects) are presented in Fig. 5. It can be observed from Fig. 5 that horizontal specimens of AlSi10Mg, Scalmalloy, QuesTek Al, and AlF357 alloys have a higher level of volumetric defects as compared to their vertical counterparts. This might be attributed to the variation in thermal history experienced by the vertical and horizontal specimens [49]. However, there is less variation in defect density of vertical and horizontal Scalmalloy and AD1 specimens; this may be ascribed to these alloys' thermal properties (e.g., thermal diffusivity, thermal conductivity). It has been reported that Al-Mg-Zr alloys have a lower thermal diffusivity, and thus, approximately ~30% lower thermal conductivity [50] as compared to Al-Si alloy systems. This lower thermal conductivity may be the reason for the lower variation in defect density between the vertical and horizontal orientations than the other alloys (see Fig. 5). Similar relatively low thermal conductivity (~30% lower than Al-Si alloys) has also been reported for the Scalmalloy [50,51]. However, it must be considered that the process parameters used to fabricate Scalmalloy were not

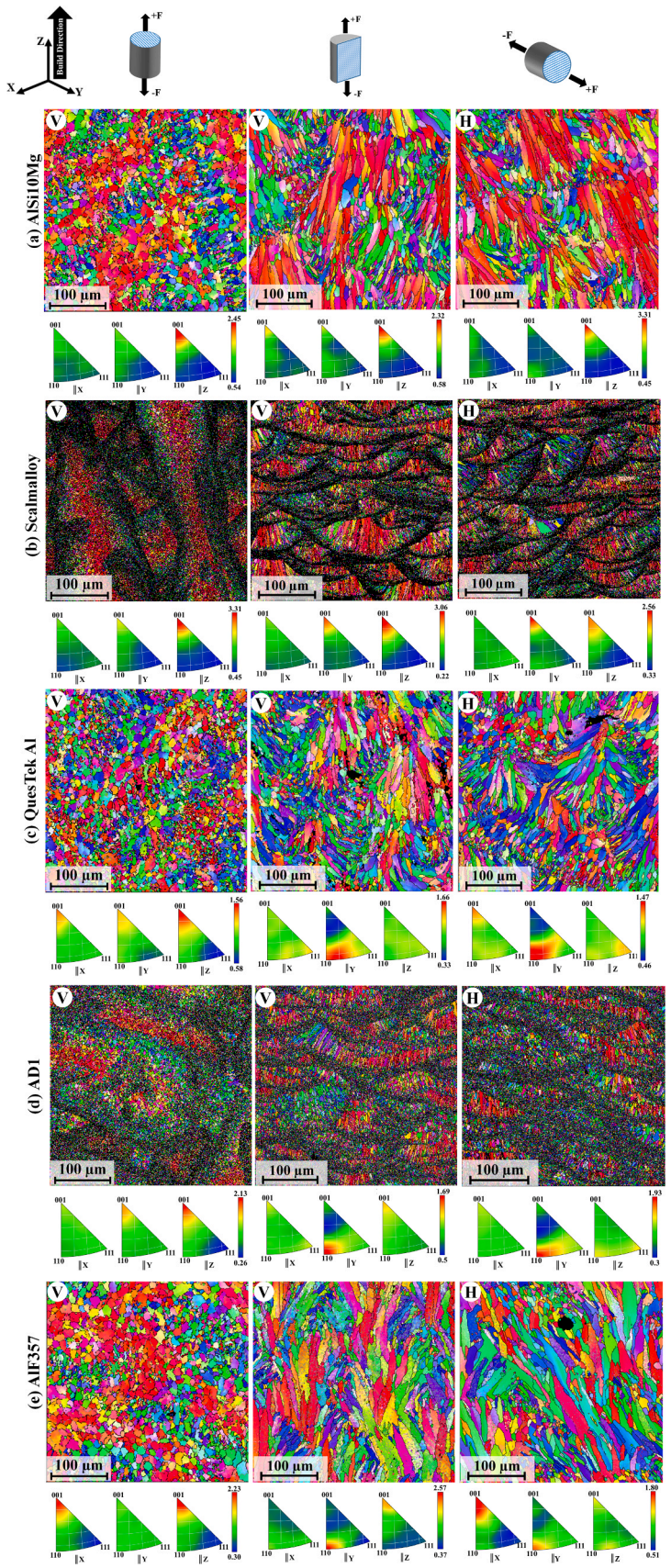

Fig. 3. Microstructure of vertical and horizontal LB-PBF Al specimens as well as the IPF sets for (a) AlSi10Mg, (b) Scalmalloy, (c) QuesTek Al, (d) AD1, and (e) AlF357.

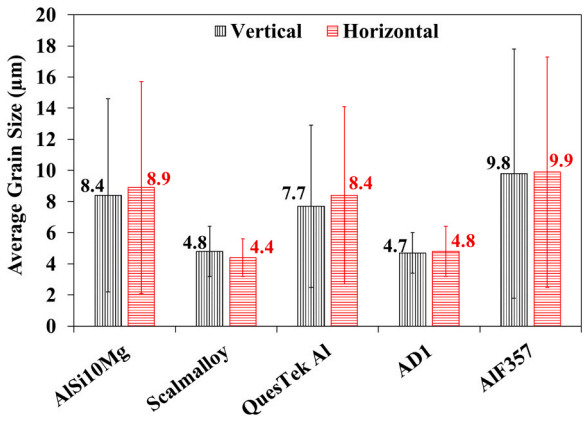

Fig. 4. The average grain size for the vertical and horizontal LB-PBF Al specimens. The standard deviation error bars are also included.

necessarily the most optimized sets, resulting in a higher porosity in these specimens. At the same time, there is less variation in defect density between vertical and horizontal Scalmalloy specimens than the AlSi10Mg, QuesTek Al, and AlF357.

Based on the results presented in Fig. 5(f), the AlSi10Mg and AD1 alloys most likely have the most optimum process parameters as their defect density is much less compared to other Al alloys. Although optimized process parameters were used, a high defect density is observed in AlF357, which may be due to its high thermal conductivity. In addition, the porosity in AlF357 may have been increased by conducting T6 heat treatment. Defanti et al. [52] reported the formation and even enlargement of volumetric defects after T6 heat treatment for the LB-PBF AlA357 alloy, which is a very similar alloy to the AlF357. It must be noted that the high defect density in QuesTek Al specimens is attributed to the fact that the process parameters used for this alloy were not necessarily the most optimized ones. However, Muhammad et al. [38] have reported acceptable fatigue behavior for the LB-PBF QuesTek Al and Scalmalloy fabricated using similar process parameters as the ones used in this study.

The volumetric defect size distribution of vertical and horizontal LB-PBF Al specimens is presented in Fig. 6. The volumetric defects are normalized by the total scanned volume. It is worth mentioning that both gas entrapped pores and LoF defects were observed in all the LB-PBF Al specimens scanned in this study. However, for the sake of simplicity and comparison, the diameter of the equivalent spherical volume of the defect is considered as the size of volumetric defects in this study for both gas entrapped pores or LoFs.

It can be seen that the most defects in all of the Al alloys are found to be in size range of [20−30) μm (note that no defect smaller than 20 μm was considered in this study), specifically for Scalmalloy, QuesTek Al, and ALF357. However, fatigue cracks intend to initiate from larger defects [53,54]. It can be seen for the vertical specimens in Fig. 6(a) that Scalmalloy and AlF357 have more defects larger than 40 μm, while the scanned QuesTek and AD1 specimens did not have any defects larger than 40 μm. The maximum defect size in the scanned vertical specimens was found to be 41, 49, 36, 35, 58 μm, respectively, for AlSi10Mg, Scalmalloy, QuesTek Al, AD1, and AlF357 scanned specimens. For the horizontal specimens in Fig. 6(b), while all the scanned specimens had defects larger than 40 μm, larger defects were found in QuesTek Al and AlF357. The maximum defect size found in the scanned horizontal specimens was 46, 51, 47, 47, 49 μm, respectively, for AlSi10Mg, Scalmalloy, QuesTek Al, AD1, and AlF357 scanned specimens.

3.3. Cyclic deformation and fatigue behavior

The stable stress-strain hysteresis loops obtained from the uniaxial fully-reversed strain-controlled fatigue tests of LB-PBF Al alloys are presented in Fig. 7. The hysteresis loops of tests performed at 0.002 mm/mm and 0.003 mm/mm strain amplitudes are shown for vertical and horizontal build orientations, separately. For the fatigue tests at 0.002 mm/mm strain amplitude (see Fig. 7(a)), all the LB-PBF Al alloys, except AlSi10Mg, exhibit elastic behavior in both vertical and horizontal build orientations. This is because the stress response at 0.002 mm/mm strain amplitude is much lower than the yield strength of Scalmalloy, QuesTek Al, AD1, and AlF357, listed in Table 4. However, the stress response of AlSi10Mg at this strain amplitude level (i.e., 0.002 mm/mm) is close to its yield strength (see Table 4), resulting in slight plastic deformation.

For the fatigue tests at 0.003 mm/mm strain amplitude (see Fig. 7 (b)), LB-PBF Scalmalloy, QuesTek Al, and AD1 show elastic behavior, while the AlSi10Mg and AlF357 alloys exhibit plastic deformation. It can be seen that the amount of plastic deformation in AlSi10Mg is higher than in AlF357. In addition, it appears that the plastic deformation in both AlSi10Mg and AlF357 is slightly higher in the horizontal specimens as compared to the vertical counterparts. This may be attributed to the crystallographic orientation of grains with respect to the loading direction in vertical and horizontal specimens.

As seen in Fig. 3(a) for AlSi10Mg, and Fig. 3(e) for AlF357, grains are $< 001 >$-oriented along the loading direction (i.e., //Z-axis) in vertical specimens, while the grains are mostly $< 110 >$-/$< 111 >$-oriented along the loading direction in horizontal specimens (i.e., //Y-axis). Since Al is a material with an FCC crystal structure, $< 110 >$ and $< 111 >$ crystallographic grain orientations in horizontal specimens are the preferred slip systems, which may result in higher plastic deformation as compared to the $< 001 >$ crystallographic grain orientation of the vertical specimens.

The fatigue results for the LB-PBF Al alloys in different build orientations are listed in Table 5, and the strain-life fatigue data for each alloy in vertical and horizontal build orientations are plotted in Fig. 8. It can be seen that there is not much variation in fatigue performance between vertical and horizontal specimens for LB-PBF AlSi10Mg (Fig. 8(a)) and AlF357 (Fig. 8(e)). For the high strength alloys (see Table 4); i.e., Scalmalloy, QuesTek Al, and AD1, although there is not much variation at the higher strain amplitude, there is some scatter in fatigue lives at the lower strain amplitude of 0.002 mm/mm (see Fig. 8(b)-(d)).

As seen, none of the vertical or horizontal specimens of AlSi10Mg (Fig. 8(a)) and AlF357 (Fig. 8(e)) reached 10^7 reversals (considered as runout in this study) at 0.002 mm/mm strain amplitude. For the QuesTek Al at 0.002 mm/mm strain amplitude, shorter fatigue lives are achieved for the vertical specimens; two out of three vertical specimens failed without reaching runout, while all the three horizontal QuesTek Al specimens exceeded 10^7 reversals. For Scalmalloy (Fig. 8(b)), one horizontal specimen, and for AD1 (Fig. 8(d)), one vertical specimen failed before 10^7 reversals, while all other vertical and horizontal specimens reached runout at 0.002 mm/mm strain amplitude. The scatter in fatigue lives of the LB-PBF Scalmalloy, QuesTek Al, and AD1 may be due to their relatively high strength making them more susceptible to the defects under cyclic loading [40].

3.4. Fatigue failure mechanisms

It is well established that the volumetric defects (i.e., pores, LoFs) are the crack initiation sources for most AM materials in the machined surface condition [26]. However, this is not the case for all AM materials; for instance, the cracks are reported to initiate from the surface, not the volumetric defects in AM IN718 machined specimens [17,55]. Therefore, it is essential to carefully investigate the failure mechanisms of the LB-PBF Al alloys in the current study. Since more scatter in fatigue results is seen in the higher cycle fatigue regime (see Fig. 8), selected fracture surfaces of vertical and horizontal LB-PBF Al specimens tested at 0.002 mm/mm strain amplitude are compared in Figs. 9 and 10, respectively. However, the defect size and type for all the failed specimens are listed in Table 5.

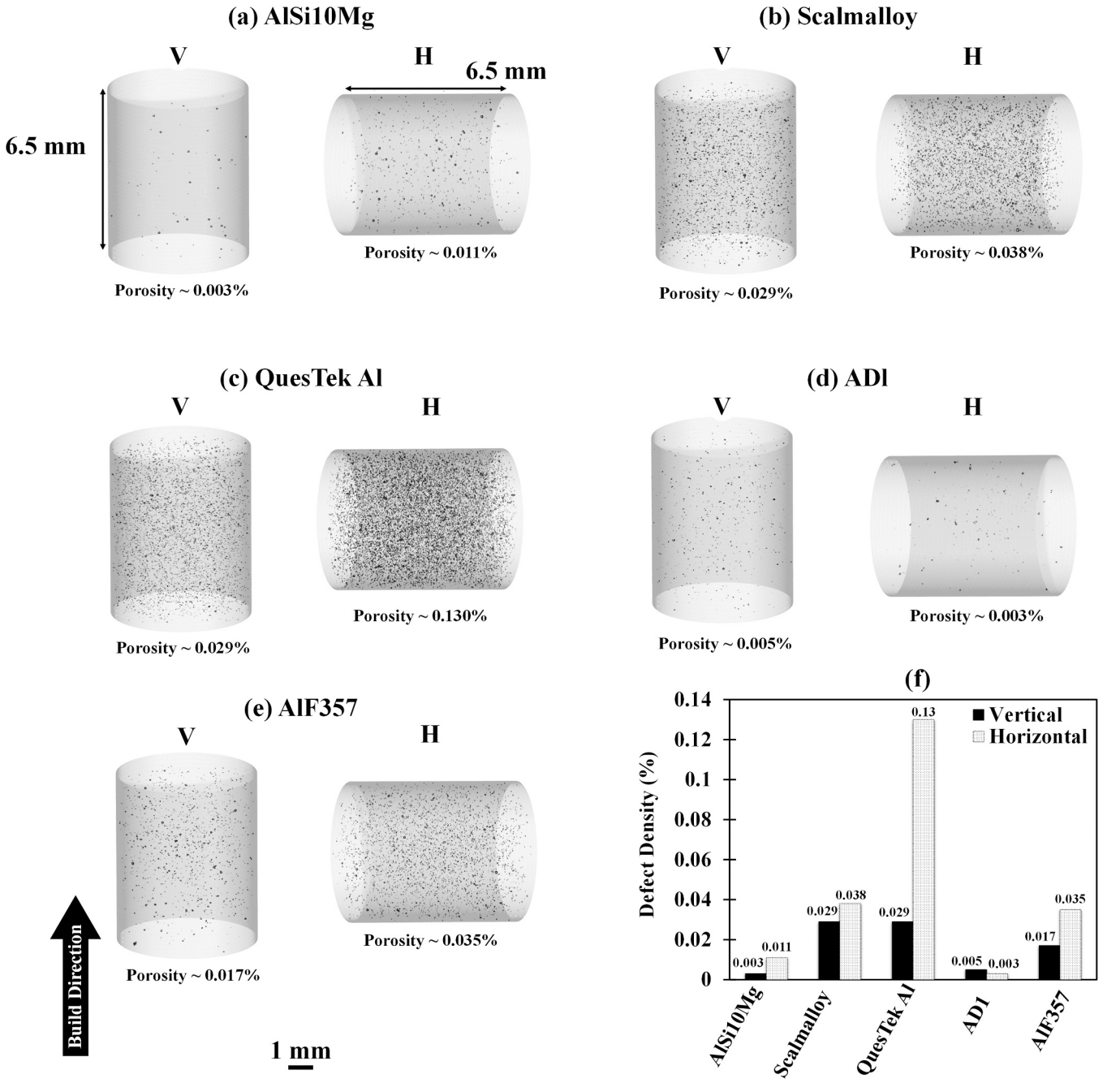

Fig. 5. X-ray CT results from a 6.5-mm length X 5-mm diameter volume in the gage section of fatigue specimens showing the porosity in vertical and horizontal LB-PBF Al specimens: (a) AlSi10Mg, (b) Scalmalloy, (c) QuesTek Al, (d) AD1, and (e) AlF357. The statistical results are shown in (f).

Note that the size of defects are analyzed by $\sqrt{area}_{Murakami}$ approach as explained in [56], and shown with green-color curves on the fracture surfaces in Figs. 9 and 10. In addition, the exact defect area is also designated on the fracture surfaces (with yellow-color curves). It must be mentioned that there is no defect size reported for the runout specimens, and some of the fracture surfaces were smashed during the test, and the defect could not be recognized. These are designated by N/A** in the table.

As seen in Fig. 9 for the vertical LB-PBF Al specimens, volumetric defects close to or on the surface, initiated the cracks in AlSi10Mg, QuesTek Al, and AlF357 alloys. Surface pores with $\sqrt{area}_{Murakami} = 31$ μm in AlSi10Mg_V2 (Fig. 9(a)) specimen and $\sqrt{area}_{Murakami} = 30$ μm in AlF357_V4 (Fig. 9(d)) specimen are noticeable. As seen, fatigue life of vertical AlF357 alloy (2 N_f = 243,092) is higher than that of vertical AlSi10Mg (2 N_f = 166,266) even with a quite similar initiating defect size in the vertical AlF357 specimen. It can be seen in Table 5 that while the defects are larger in AlF357 specimens compared to the AlSi10Mg ones (see also Figs. 5 and 6), longer fatigue lives are obtained, which may indicate more tolerance of AlF357 to the presence of defects. In other words, if process parameters and heat treatment for AlF357 are further optimized to have similar pore size distribution as AlSi10Mg, the AlF357 specimens are expected to last longer under fatigue loading.

For the QuesTek Al_V2 specimen, it is seen that the crack initiated from an LoF defect with $\sqrt{area}_{Murakami} = 59$ μm. Interestingly, the fatigue life is somehow comparable with that of vertical AlSi10Mg, even though the defect size that initiated the crack in the QuesTek Al is larger than that of AlSi10Mg. Besides, one of the QuesTek Al specimens

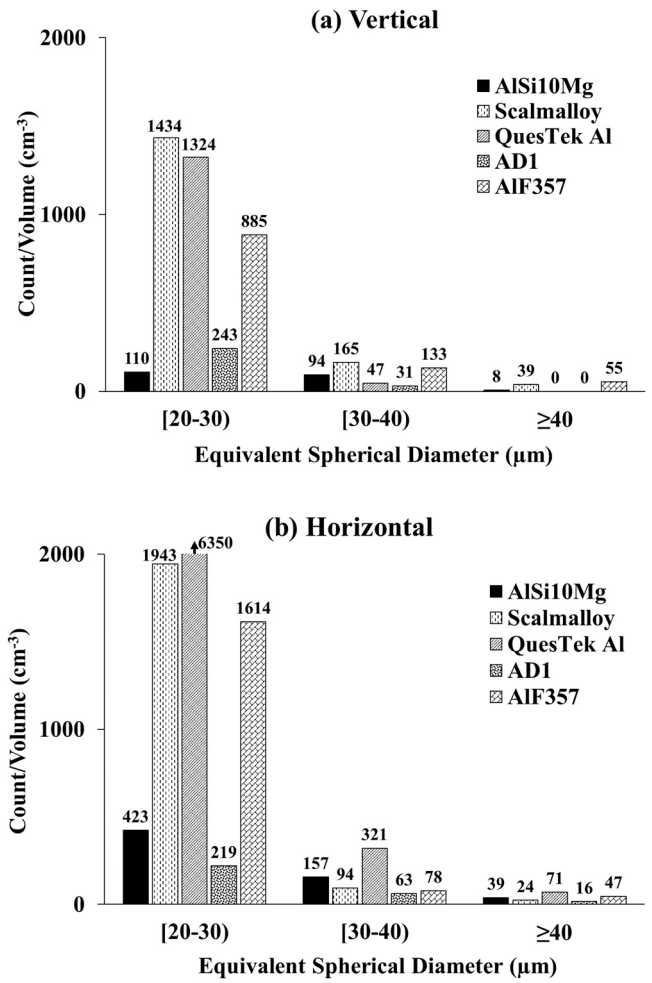

Fig. 6. Volumetric defects size distribution of (a) vertical, and (b) horizontal LB-PBF Al specimens.

reached runout, while having more porosity as compared to AlSi10Mg (see Figs. 5 and 6); therefore, the QuesTek Al may exhibit higher fatigue resistance than that of AlSi10Mg if the process parameters for QuesTek Al are better optimized. It was shown in [38] that the LB-PBF QuesTek Al had relatively high fatigue crack initiation resistance associated with its fine microstructure; however, because of its high strength, low ductility, and high porosity, more scatter in fatigue data was reported. Similarly, some considerable scatter in fatigue data of QuesTek Al is noticeable in Fig. 8.

As seen in Fig. 9(c), cracks initiated from the surface of the vertical AD1 specimen, while the other two vertical AD1 specimens reached runout at this strain amplitude level (i.e., 0.002 mm/mm). Note that AD1 specimens had relatively low porosity as compared to other Al alloys in this study (see Figs. 5 and 6). This may have shifted the crack initiation from volumetric defects to surface initiation in the absence of a relatively large defect in the vicinity of the surface. Finally, no vertical Scalmalloy specimen failed at the strain amplitude of 0.002 mm/mm, and they all reached 10^7 reversals, where the fatigue tests were suspended.

The fracture surfaces of selected horizontal LB-PBF Al specimens tested at 0.002 mm/mm strain amplitude are shown in Fig. 10. It is worth noting that all the horizontal AD1 and QuesTek Al specimens reached runout at this strain amplitude. It can be seen in Fig. 10(a) that two surface LoF defects with $\sqrt{area}_{Murakami}$ = 30 µm and 40 µm initiated the cracks in the AlSi10Mg_H4 specimen. Among all the horizontal Scalmalloy specimens, only one specimen failed before reaching runout, for which the fracture surface is presented in Fig. 10(b). As observed, a very large LoF defect with $\sqrt{area}_{Murakami}$ = 102 µm caused failure of the Scalmalloy_H2 specimen. Interestingly enough, even with this large LoF defect, the fatigue life of Scalmalloy_H2 is longer than those of AlSi10Mg_H4, and AlF357_H2 specimens. This is associated with the high fracture toughness of Scalmalloy resulting from its combined high strength and high ductility associated with its nano-size grain structure (see Fig. 3(b)). It is worth noting that the process parameters utilized to fabricate Scalmalloy may have not necessarily been the optimized ones; therefore, if the process parameters are further optimized to reducing the volumetric defects in Scalmalloy, much enhancement in fatigue behavior of this alloy is expected. For the LB-PBF AlF357_H2 specimen shown in Fig. 3(c), a LoF defect with $\sqrt{area}_{Murakami}$ = 47 µm initiated the crack. Although the defect size is again much smaller than the one in the Scalmalloy specimen (Fig. 3(b)), the AlF357_H2 specimen failed at a shorter fatigue life.

In some cases listed in Table 5, mainly for the specimens tested at the higher strain amplitude of 0.003 mm/mm, cracks initiated from the surface rather than a volumetric defect. These specimens were either the ones with low defect density, e.g., AD1_V2, or in rare cases, the volumetric defect was further away from the surface, e.g., AlSi10Mg_H3. In such cases, the intrusion/extrusion most likely formed and initiated the crack at the surface of the specimen [57].

4. Discussion on experimental results

In this section, fatigue behaviors of LB-PBF Al alloys are compared and discussed with respect to their micro-/defect-structure. In addition, build orientation dependency in fatigue behavior of LB-PBF Al alloys is further evaluated.

4.1. Potential anisotropy in fatigue behavior

Fatigue behavior of AM materials can vary based on the build orientation due to the micro-/defect-structure anisotropy induced by AM processes [58]. The thermal history experienced by parts fabricated in different build orientations is not necessarily identical and can be affected by time interval and geometrical factors [59–61]. The gage section of horizontally built specimens usually is closer to the build platform than the one for the vertically built specimens, which may lead to faster heat dissipation in horizontal specimens. The higher cooling and solidification rates may result in horizontally built parts having more volumetric defects than the vertical ones, which is confirmed in Fig. 5.

The difference between the defect density in vertical and horizontal specimens may cause anisotropy in fatigue behavior. Although it can be seen in Fig. 8 that there is not much anisotropy in the fatigue performance of LB-PBF Al alloys at the higher strain amplitude of 0.003 mm/mm, it appears to be some level of anisotropy in the fatigue behavior at the lower strain amplitude of 0.002 mm/mm. To clarify whether this is anisotropy or scatter in fatigue lives, the fatigue data of vertical and horizontal LB-PBF Al specimens tested at 0.002 mm/mm strain amplitude are presented via box plots in Fig. 11. It must be noted that the runout tests, with their terminated number of reversals listed in Table 5, are also included in statistical analysis and shown by black arrows.

It is worth noting that the difference between the upper and lower quartiles represents the scatter in fatigue lives, while the difference between the fatigue life median for the vertical and horizontal specimens shows the anisotropy in fatigue behavior. As seen, there is more scatter in fatigue lives of horizontal specimens in most cases (i.e., AlSi10Mg, Scalmalloy, and AlF357), which can be explained by the higher defect density in their horizontal specimens compared to the vertical ones (see Fig. 5). However, since the defect density is relatively low in the horizontal AD1 specimens (Fig. 5(d)), there is not much scatter in its fatigue lives. Only one outlier vertical AD1 specimen caused scatter in fatigue lives of the vertical AD1 specimens (see Fig. 8). On the

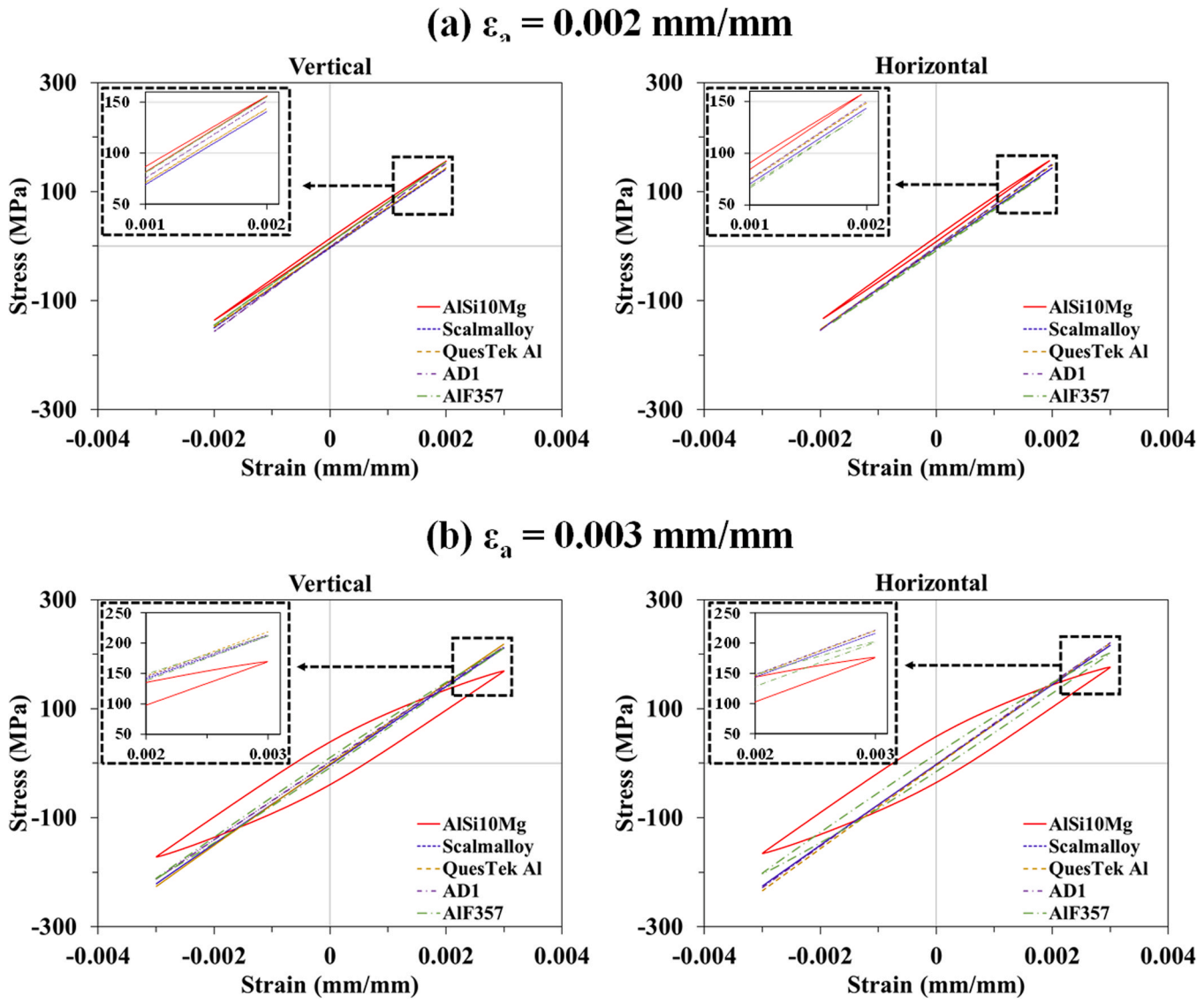

Fig. 7. Stable hysteresis loops of fully-reversed strain-controlled constant amplitude fatigue tests of vertical and horizontal LB-PBF Al specimens at (a) 0.002 mm/mm, and (b) 0.003 mm/mm strain amplitudes.

other hand, it can be seen in Fig. 11 that, the LB-PBF AlSi10Mg, Scalmalloy, and AD1 specimens have somewhat comparable fatigue life medians for vertical and horizontal specimens, confirming no anisotropy in their fatigue behavior.

Although more defects are present in the horizontal specimens (see Fig. 5), which are expected to deteriorate the fatigue behavior, one may wonder why the horizontal AlSi10Mg, Scalmalloy, and AD1 specimens have comparable median fatigue lives to their vertical counterparts (see Fig. 11). This may be explained by the size of the projected area of the defects (particularly in the presence of LoF defects on the loading plane) in horizontal specimens, which may compensate for the detrimental effect of high defect density in these specimens. The projected area of the LoF defects on the loading plane of the horizontal specimens is often smaller than those in the vertical specimens [6,62], as can be seen in Table 5. The LoF defects, which are formed either between subsequent layers or adjacent tracks, typically have a slit shape, and their wider area is parallel to the loading direction in horizontal specimens, while they are perpendicular to the loading direction in vertical specimens [58]. The larger projected area of LoF defects in vertical specimens can result in higher stress concentrations, and consequently, deterioration of the fatigue strength in vertical specimens. Accordingly, comparable fatigue lives may be obtained despite higher defect density in horizontal specimens compared to their vertical counterparts.

The fatigue life median for the horizontal AlF357 specimens in Fig. 11 is slightly lower than that of the vertical ones, which shows slight anisotropy in the fatigue behavior of this alloy. This is due to the type of defects (i.e., pore vs. LoF) that initiated the cracks in the vertical and horizontal AlF357 specimens. As seen in Table 5, the cracks initiated from the spherical pores in the vertical AlF357 specimens, while LoF defects caused failure in the horizontal counterparts. It is known that the larger LoF defects are typically more detrimental than smaller spherical pores to the fatigue life; nonetheless, the projected area of the LoF defects on the loading plane of the horizontal AlF357 specimens is not considerably larger than the pores seen on the fracture surface of vertical specimens (see Table 5). As a result, the anisotropy in the fatigue behavior of AlF357 is not significant.

On the other hand, for the QuesTek Al alloy in Fig. 11, the fatigue life median in vertical specimens is considerably (one order of magnitude) lower than the horizontal ones; this may represent anisotropy in the fatigue behavior. As seen in Table 5, the cracks initiated from LoF defects for the vertical QuesTek Al specimens tested at 0.002 mm/mm strain amplitude, while all the horizontal specimens reached runout at

Table 5
Uniaxial fully-reversed strain-controlled fatigue data of LB-PBF Al alloys generated in this study, along with the information of the crack-initiating defects (i.e., size, type, and location) for each specimen.

	Build orientation	ID	ε_a (mm/mm)	σ_a (MPa)	σ_m (MPa)	$2N_f$ (Reversals)	$\sqrt{area}_{Murakami}$ defect (s) (μm)	Location/Type
AlSi10Mg	Vertical	V2	0.002	147	-4	185,004	31	Surface[a]/Pore
		V4	0.002	146	10	166,266	40	Surface/LoF
		V6	0.002	145	-1	157,570	49	Surface/LoF
		V1	0.003	171	-1	27,118	N/A	N/A[b]
		V5	0.003	169	2	23,978	56	Surface/LoF
		V3	0.003	174	-2	9378	N/A	Intrusion/extrusion
	Horizontal	H2	0.002	147	17	209,086	N/A	N/A[b]
		H4	0.002	147	14	145,400	40, 30	Surface/LoFs
		H6	0.002	146	-2	78,266	N/A	N/A[b]
		H5	0.003	171	2	25,416	51	Surface/Pore
		H1	0.003	171	5	25,096	48	Surface/LoF
		H3	0.003	177	4	20,992	N/A	Intrusion/extrusion
Scalmalloy	Vertical	V2	0.002	145	-4	> 11,122,572	N/A	N/A
		V4	0.002	144	2	> 10,110,224	N/A	N/A
		V6	0.002	144	2	> 12,625,074	N/A	N/A
		V5	0.003	217	-9	143,452	49	Surface /Pore
		V3	0.003	214	0	117,042	69	Surface /Pore
		V1	0.003	216	-4	76,908	75	Surface /Pore
	Horizontal	H6	0.002	145	-4	> 13,937,622	N/A	N/A
		H4	0.002	146	-5	> 10,085,040	N/A	N/A
		H2	0.002	148	-5	197,030	102	Surface/LoF
		H1	0.003	221	-4	60,648	55	Surface/LoF
		H5	0.003	219	-2	77,774	57	Surface/LoF
		H3	0.003	217	-4	35,918	N/A	N/A[b]
QuesTek Al	Vertical	V4	0.002	148	0	> 11,562,816	N/A	N/A
		V6	0.002	147	-4	762,790	87	Surface/LoF
		V2	0.002	146	-2	176,582	59	Surface/LoF
		V5	0.003	224	-4	90,244	55	Surface/Pore
		V1	0.003	220	-10	63,540	66	Surface/LoF
		V3	0.003	222	-4	62,668	33, 31	Surface/LoF
	Horizontal	H2	0.002	149	0	> 11,545,714	N/A	N/A
		H4	0.002	150	-2	> 10,760,842	N/A	N/A
		H6	0.002	147	-1	> 10,000,000	N/A	N/A
		H3	0.003	221	-3	105,310	55	Surface/LoF
		H5	0.003	225	-4	82,364	63	Surface/LoF
		H1	0.003	227	-6	65,502	64	Surface/LoF
AD1	Vertical	V6	0.002	147	-3	> 12,326,510	N/A	N/A
		V4	0.002	150	-2	> 11,668,896	N/A	N/A
		V2	0.002	154	-3	290,658	N/A	Intrusion/extrusion
		V5	0.003	228	-5	169,838	41	Surface/Pore
		V1	0.003	213	-1	104,220	40	Surface/Pore
		V3	0.003	225	-6	93,412	104	Surface/LoF
	Horizontal	H4	0.002	153	-1	> 11,532,228	N/A	N/A
		H2	0.002	153	-2	> 10,325,838	N/A	N/A
		H6	0.002	143	-1	> 10,000,000	N/A	N/A
		H5	0.003	229	4	191,144	38	Surface/Pore
		H1	0.003	218	-1	143,822	42	Surface/Pore
		H3	0.003	226	-4	140,644	44	Sub-surface/Pore
AlF357	Vertical	V6	0.002	145	-1	292,060	40	Surface/Pore
		V2	0.002	150	5	276,004	29	Surface/Pore
		V4	0.002	141	12	243,092	30	Surface/Pore
		V3	0.003	209	0	31,006	N/A	N/A[b]
		V1	0.003	212	2	23,060	N/A	N/A[b]
		V5	0.003	208	2	14,652	N/A	N/A[b]
	Horizontal	H4	0.002	146	7	192,176	43	Surface/LoF
		H2	0.002	136	-7	106,692	47	Surface/LoF
		H6	0.002	152	-15	53,578	N/A	N/A[b]
		H3	0.003	204	-3	27,680	48	Surface/LoF
		H5	0.003	208	8	12,150	N/A	N/A[b]
		H1	0.003	202	0	15,814	N/A	N/A[b]

[a] Cracks initiated from defects located at or adjacent to the surface are defined as "*Surface pore/LoF*".
[b] The fracture surface was damaged.

this level. Although the horizontal QuesTek Al specimens have a higher defect density than the vertical ones (see Fig. 6(c)), the projected area of the LoF defects on the loading plane should have been smaller than those of vertical specimens, resulting in superior fatigue performance of horizontal specimens.

In addition to the role of defects on the fatigue anisotropy of LB-PBF Al alloys studied here, the role of microstructure, particularly the crystallographic orientation of the grains, should be considered. While shown in Fig. 3 that the grain structure (i.e., size and morphology of grains) has not been much affected by the build orientation, the preferred crystallographic orientation of grains with respect to the loading direction is different between the vertical and horizontal specimens. The crystallographic orientation of grains towards the loading direction in horizontal LB-PBF AlSi10Mg, QuesTek Al, AD1, and AlF357specimens is < 011 > and < 111 > (see //Y-axis IPF in Fig. 3), and for horizontal Scalmalloy, there are also grains oriented along

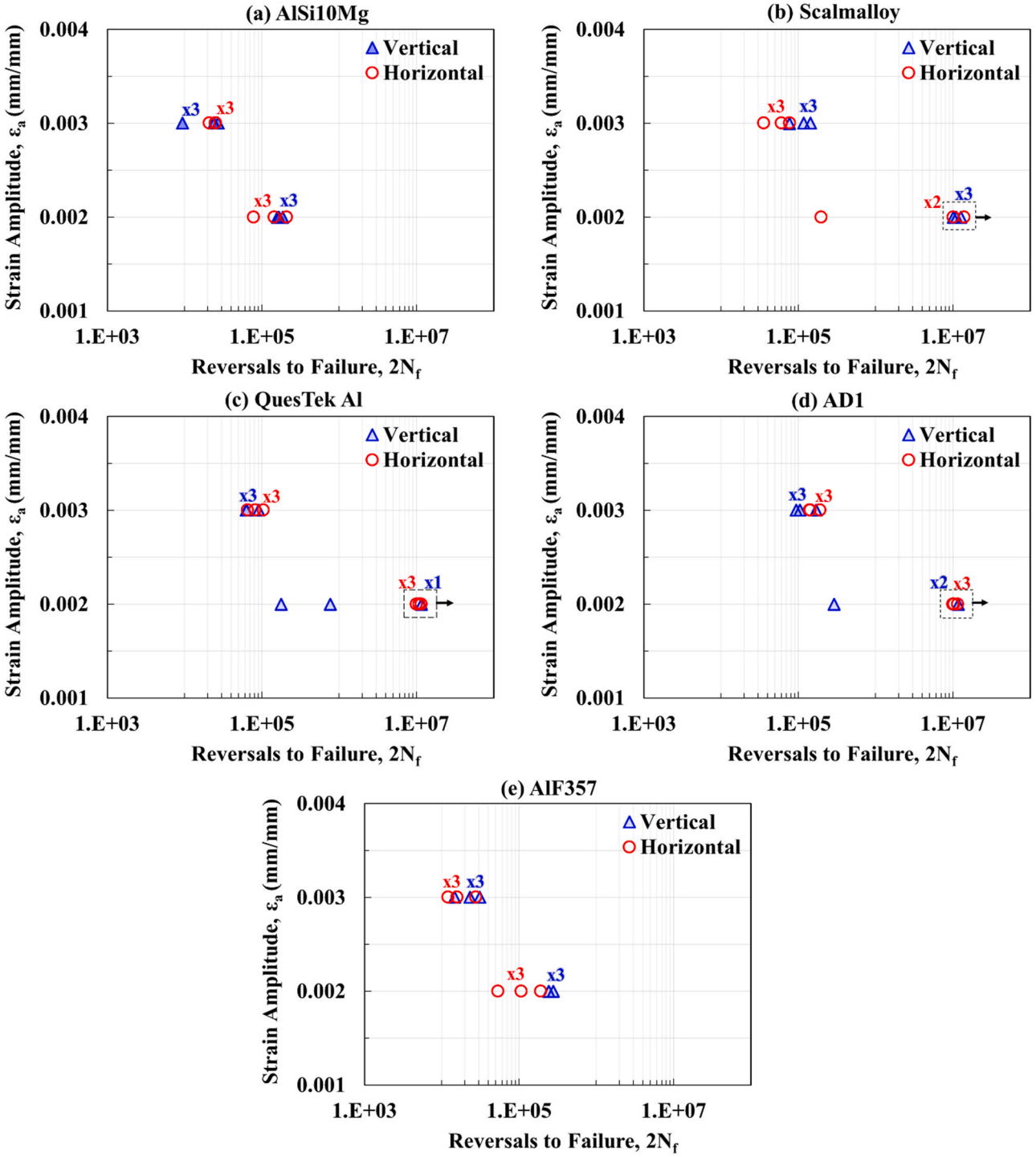

Fig. 8. Strain-life fatigue comparison of vertical and horizontal LB-PBF Al specimens: (a) AlSi10Mg, (b) Scalmalloy, (c) QuesTek Al, (d) AD1, and (e) AlF357.

< 001 >. On the other hand, the grains are mainly < 001 >-oriented in the vertical specimens (see //Z-IPF in Fig. 3), except for the vertical QuesTek Al and AD1 specimens with randomly-oriented grains. Nevertheless, considering the easier cross slip along < 011 > and < 111 > orientations rather than < 001 > in FCC materials, a more ductile behavior is expected for the horizontal AlSi10Mg, QuesTek Al, AD1, and AlF357 specimens (see Table 4 and Fig. 7), which can result in less sensitivity of these materials to the presence of defects.

It can be concluded that the smaller projected area of LoF defects on the loading plane of horizontal specimens can lower the stress concentration, and the preferred < 011 > and < 111 > orientation of the grains can reduce the material's sensitivity to defects. These may assist the horizontal AlSi10Mg specimens while having more volumetric defects, exhibit a comparable fatigue resistance to the vertical ones. Although QuesTek Al is much sensitive to the presence of defects due to its high strength and low ductility, the combined effect of the smaller projected area of LoF defects on the loading plane of the horizontal specimens and the preferred < 011 > and < 111 > orientation of grains in horizontal specimens, can improve the fatigue behavior of horizontal specimens as compared to the vertical ones.

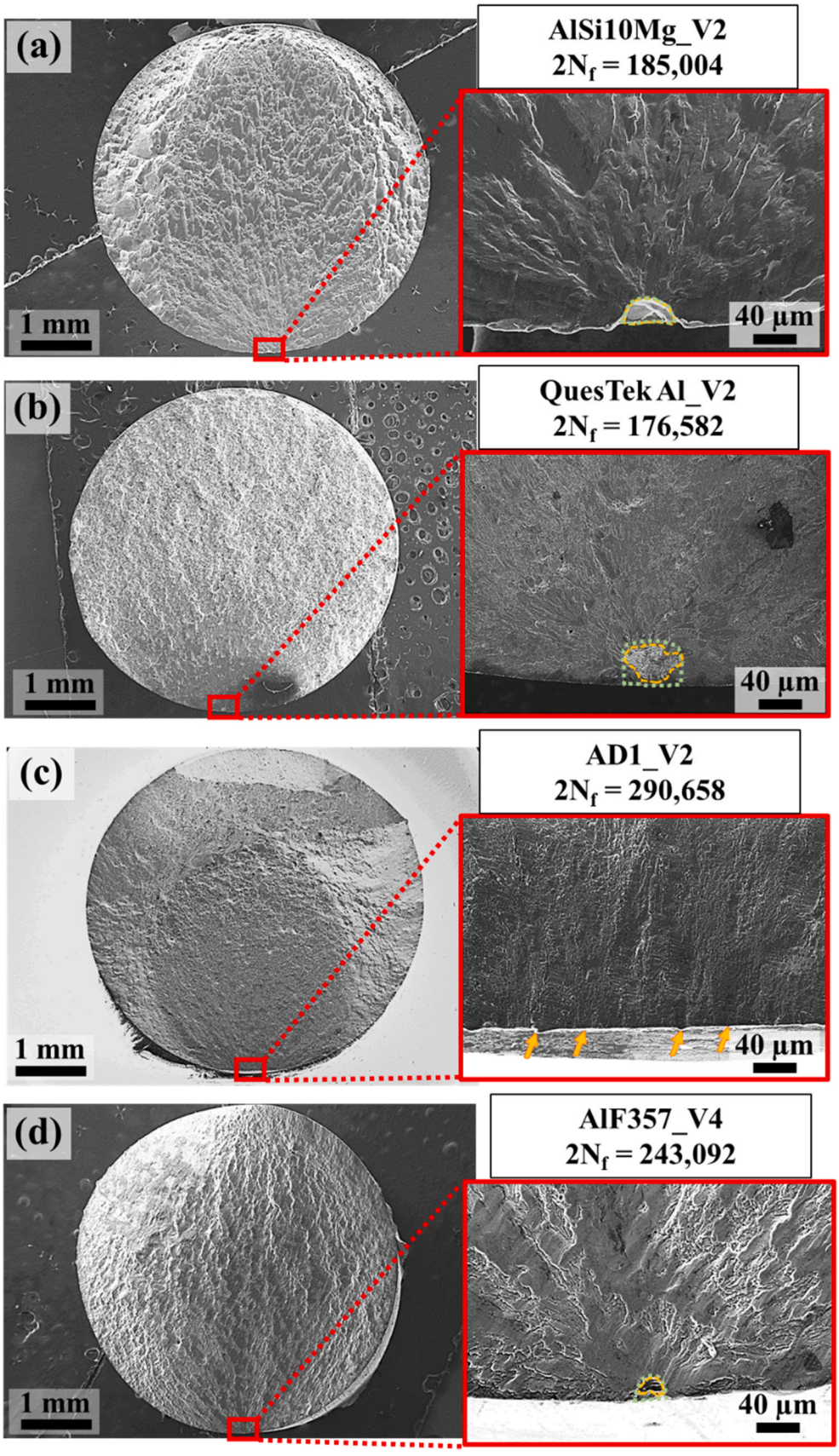

Fig. 9. Fracture surfaces of vertical LB-PBF Al specimens tested at 0.002 mm/mm strain amplitude: (a) AlSi10Mg, (b) QuesTek Al, (c) AD1, and (d) AlF357. Note that all vertical Scalmalloy specimens reached runout at this strain amplitude.

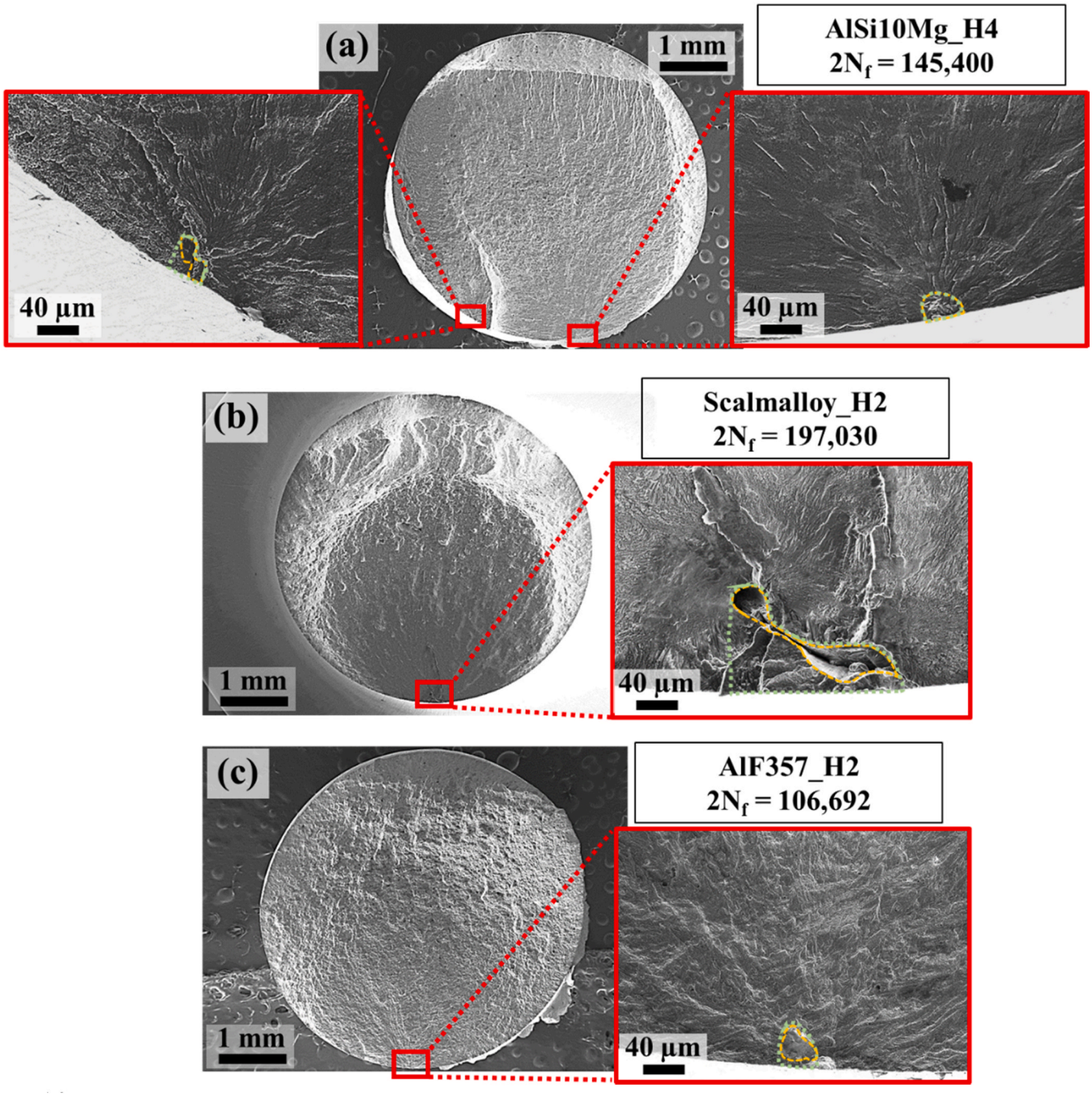

Fig. 10. Fracture surfaces of horizontal LB-PBF Al specimens tested at 0.002 mm/mm strain amplitude: (a) AlSi10Mg, (b) Scalmalloy, and (c) AlF357. Note that all the horizontal QuesTek Al and AD1 specimens reached runout at this strain amplitude.

4.2. Comparing fatigue behavior of Al alloys

Strain-life and stress-life fatigue behavior of vertical LB-PBF Al specimens are presented in Fig. 12(a) and (b), respectively. It can be seen that the LB-PBF AlSi10Mg and AlF357 alloys have somewhat similar strain-life fatigue behaviors, while AlF357 has a higher stress-life fatigue behavior at 0.003 mm/mm than AlSi10Mg (see Fig. 12(b)). This can be explained by the slightly higher strength of AlF357 compared to AlSi10Mg (see Table 4) and the plastic deformation of AlSi10Mg at 0.003 mm/mm strain amplitude (see Fig. 7). Accordingly, AlF357 may be more favorable for load-bearing applications than AlSi10Mg alloy.

The higher level of defects in AlF357 as compared to AlSi10Mg (see Fig. 5) is expected to make this material (i.e., AlF357) more prone to failure, and consequently, decrease its fatigue strength as compared to AlSi10Mg. Nevertheless, similar fatigue lives of AlF357 and AlSi10Mg may be associated with their different microstructure characteristics. The stress relief cycle applied on the AlSi10Mg has been found insufficient to remove the brittle intercellular Si network in the microstructure [38], while the solution homogenizing heat treatment performed on AlF357 alloy removes the brittle intercellular Si network in the microstructure [21]. Since intercellular Si networks in the microstructure result in premature cracking and lower crack growth resistance of the material [38], removal of the Si network is found to assist with improving the fatigue behavior. Therefore, the detrimental effect of the high level of defects in AlF357 may have been compensated by its enhanced microstructure (i.e., absence of intercellular Si network) after

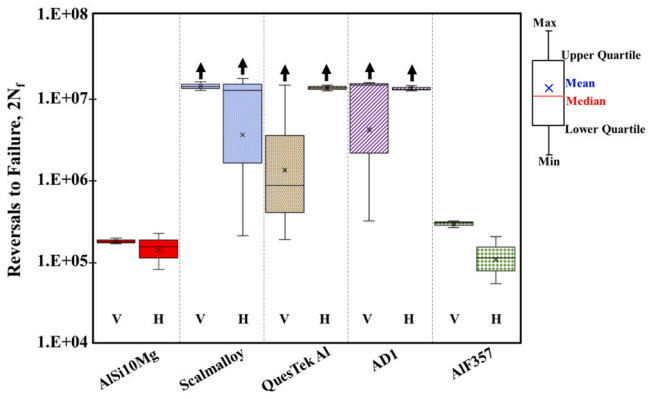

Fig. 11. Fatigue data of vertical and horizontal LB-PBF Al specimens, tested at 0.002 mm/mm strain amplitude, shown in box and whisker plots. Note that the arrows indicate the runout.

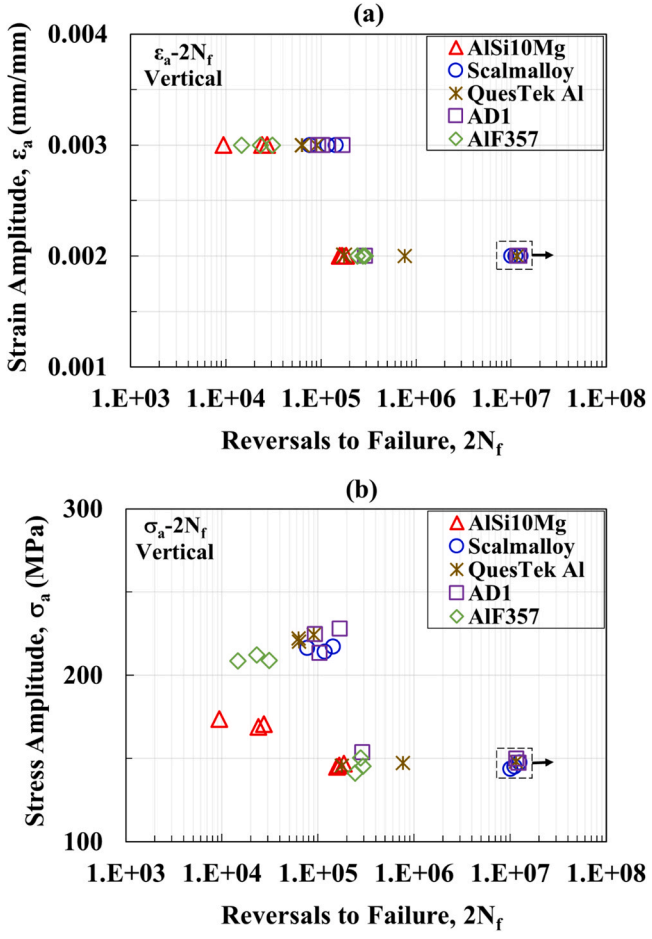

Fig. 12. (a) Strain-life, and (b) stress-life fatigue behavior of vertical LB-PBF Al specimens.

heat treatment resulting in comparable fatigue resistance to that of AlSi10Mg.

As seen in Fig. 12(a) and (b), the vertical LB-PBF Scalmalloy, QuesTek Al, and AD1 specimens have higher fatigue resistance than AlSi10Mg and AlF357 specimens, which is associated with their higher strength (see Table 4) and finer microstructure (see Fig. 3) as compared to AlSi10Mg and AlF357 alloys. The heat treatments applied on the Scalmalloy and AD1 increase their strength due to the newly formed nano-size Al_3Sc and Al_3Zr precipitates, respectively [36]. In addition, the nano-size precipitates formed during fabrication are coarsened, which enhances the ductility; therefore, the high strength and ductility of the Scalmalloy and AD1 specimens can potentially result in an enhanced fatigue performance of these materials compared to AlSi10Mg, QuesTek Al, and AlF357. In the case of QuesTek Al, it has been reported that the possible formation of SiO_2 by the heat treatment applied (see Table 3) can increase the static strength of the material, while reduces its ductility [38]. This results in higher sensitivity of this material to the defects particularly in HCF regime.

The LB-PBF Scalmalloy, QuesTek Al, and AD1 specimens have similar fatigue resistance at 0.003 mm/mm strain amplitude. However, there is variation in their fatigue lives at 0.002 mm/mm strain amplitude; all the vertical Scalmalloy specimens reached runout, while one specimen out of three from AD1, and two specimens out of three from QuesTek Al specimens failed. Since the Scalmalloy, QuesTek Al, and AD1 are high-strength alloys, they are more sensitive to defects in the HCF regime.

The average size of the crack-initiating defects in Scalmalloy, QuesTek Al, and AD1 vertical specimens are fairly similar; ~ 54 μm, 60 μm, and 62 μm, respectively. Although the vertical Scalmalloy has a higher defect density than the vertical AD1, they have comparable fatigue lives. Therefore, it is postulated that the Scalmalloy would outperform the AD1 if its process parameters are better optimized. In the case of Scalmalloy and AD1, however, the combination of their high strength and high ductility may result in higher fracture toughness, and consequently, higher fatigue resistance as compared to QuesTek Al. On the other hand, the scatter in fatigue results of vertical QuesTek Al specimens at 0.002 mm/mm is ascribed to its high strength and low ductility, which makes this material the most sensitive to the presence of defects (see Fig. 5). Similar scatter in fatigue results have been reported for LB-PBF QuesTek Al alloy in [38]. Further optimizing the process parameters for QuesTek Al may diminish the scatter in fatigue data and perhaps the anisotropy discussed in the previous section.

Strain-life and stress-life fatigue data of horizontal LB-PBF Al specimens are compared in Fig. 13(a) and (b), respectively. Similar to the vertical specimens, horizontal AlSi10Mg, and AlF357 alloys exhibit comparable fatigue lives in all strain amplitude levels, while AlF357 exhibits a higher stress response at 0.003 mm/mm strain amplitude (Fig. 13(b)). Among the high strength LB-PBF Al alloys, the fatigue resistance of Scalmalloy is apparently slightly lower than that of AD1 in the horizontal build orientation at 0.003 mm/mm strain amplitude. This can be associated with the crystallographic orientation of grains with respect to the loading direction (see //Y-axis IPF in Fig. 3) and the differences in their porosity level (Scalmalloy has a higher defect density than AD1, as seen in Fig. 5).

As seen in the //Y-axis IPF of horizontal Scalmalloy in Fig. 3(b), there is a texture along < 001 > direction, while for the horizontal AD1 the grains are strongly < 011 >- and < 111 >- oriented (i.e., the easy cross slip for FCC structure). Therefore, the horizontal AD1 specimen is expected to have more ductile behavior under cyclic loading as compared to the horizontal Scalmalloy. It can also be seen in Table 4 that the horizontal AD1 possesses higher ductility than the horizontal Scalmalloy, which makes it less sensitive to the presence of defects compared to the Scalmalloy. The horizontal AD1 specimens also have a lower level of defects in the structure as compared to the horizontal Scalmalloy specimens (compare Fig. 5(d) and (b)). Therefore, considering the preferred < 011 > and < 111 > crystallographic orientation of the grains as well as the lower level of defects and less sensitivity to the presence of defects, the horizontal AD1 specimens outperform the horizontal Scalmalloy specimens.

While all the horizontal QuesTek Al and AD1 specimens reached runout at 0.002 mm/mm strain amplitude, one out of the three horizontal Scalmalloy specimens failed without reaching runout (i.e., 10^7 reversals). The failure in this specimen occurred by a large LoF defect (102 μm) shown in Fig. 11(b). Although the projected area of the LoF defects on the loading plane of the horizontal specimens are supposedly

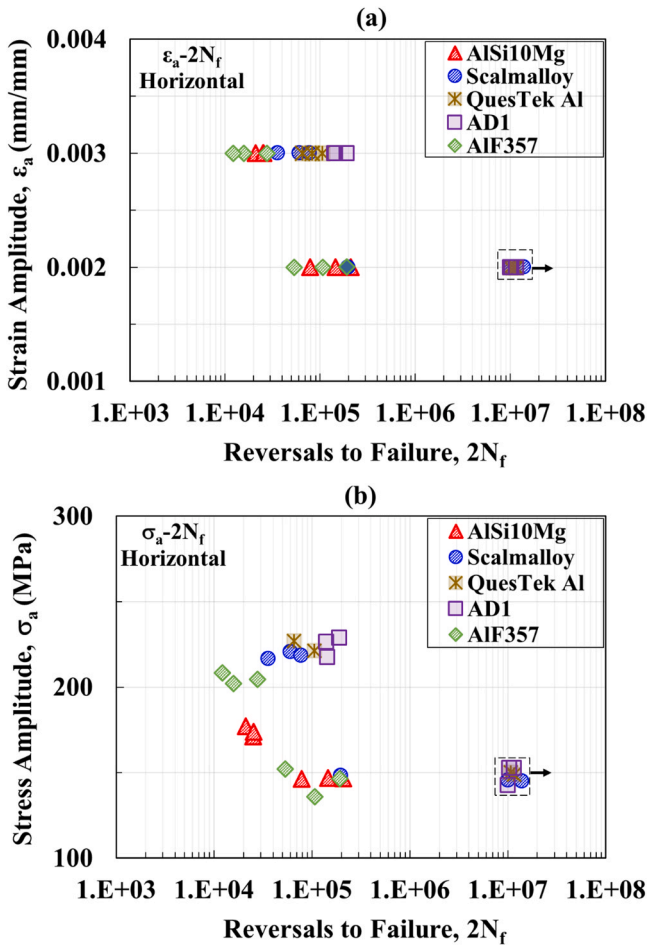

Fig. 13. (a) Strain-life, and (b) stress-life fatigue behavior of horizontal LB-PBF Al specimens.

smaller than those in the vertical counterparts, in the presence of a very large LoF defect in the horizontal specimens, the projected area on the loading plane can be still large enough to cause fatigue failure. This scatter in fatigue behavior of Scalmalloy is due to more and larger defects in this material ascribed by the fact that the employed process parameters for fabricating these specimens were not necessarily the most optimized ones. Interestingly enough, the fatigue life of the failed horizontal Scalmalloy specimen is comparable to the AlSi10Mg and AlF357 specimens with much smaller defects responsible for their fatigue failure (average crack-initiating defects in AlSi10Mg and AlF357 horizontal specimens at 0.002 mm/mm strain amplitude were 40 μm and 45 μm, respectively). This indicates higher fatigue resistance of LB-PBF Scalmalloy as compared to the AlSi10Mg and AlF357 alloys when they all have the same porosity level. Therefore, the fatigue behavior of Scalmalloy specimens is expected to be improved even further by optimizing the manufacturing process parameters.

5. Conclusions

In this study, micro-/defect-structure and fatigue behavior of five different LB-PBF Al alloys (i.e., AlSi10Mg, Scalmalloy, QuesTek Al, AD1, and AlF357) fabricated in both vertical and horizontal orientations were investigated. The fatigue behavior of each alloy in each build orientation was attempted to be correlated to its micro-/defect-structure. The following conclusions are based on the experimental observations in this study:

1. The grain structure (i.e., size and morphology of grains) was not much affected by the build orientation; however, the preferred crystallographic orientation of grains with respect to the loading direction was different between the vertical and horizontal specimens. The grains were mainly < 011 >- and < 111 >-oriented (i.e., the easy cross slip for FCC structure) in horizontal specimens, except for the horizontal Scalmalloy in which grains were also < 001 >-oriented. On the other hand, grains were < 001 >-oriented in vertical specimens, except for the vertical QuesTek Al and AD1 that possessed randomly oriented grains.
2. A higher level of volumetric defects was observed for the horizontal LB-PBF Al specimens than the vertical counterparts. However, Scalmalloy and AD1 had the lowest variation in defect density between the vertical and horizontal specimens. This was explained by the lower thermal conductivity of these alloys (~30% lower than that of Al-Si alloys). However, the Scalmalloy specimens had a high defect density, which was ascribed to the non-optimized process parameters used for their fabrication.
3. There was no significant build orientation dependency seen in fatigue behavior of LB-PBF Al specimens at the higher strain amplitude of 0.003 mm/mm. However, the AlF357 and QuesTek Al specimens showed anisotropy in fatigue behavior at 0.002 mm/mm strain amplitude.
4. The differences in defect type (i.e., pore, LoF) and size between the vertical and horizontal specimens caused anisotropy in the fatigue behavior of AlF357 and QuesTek Al alloys. The slightly better fatigue performance of vertical AlF357 specimens was due to crack initiation from small pores compared to the large LoF defects in horizontal specimens. For the QuesTek Al, the larger projected area of LoF defects on the loading plane of the vertical specimens caused them to have shorter fatigue lives than the horizontal specimens.
5. The LB-PBF AD1 specimens outperformed AlSi10Mg, QuesTek Al, and AlF357 specimens in fatigue performance regardless of the build orientation. This was due to the lower defect density, high tensile strength (higher than AlSi10Mg and AlF357, and somewhat comparable with QuesTek Al), and higher %El of AD1 compared to the other alloys.
6. The vertical Scalmalloy specimens had comparable fatigue lives to vertical AD1 specimens, while horizontal Scalmalloy specimens exhibited slightly inferior fatigue performance than horizontal AD1 specimens. The high intensity of < 001 > -oriented grains and low intensity of < 011 >- and < 111 >-oriented grains as well as the presence of more defects in the horizontal Scalmalloy specimens, made them more prone to fatigue failure as compared to the horizontal AD1 specimens.

One of the gaps with high priority in the AMSC road map [39] is related to the generation of the material properties database. This leads to further adoption of AM in load-bearing applications and helps with enabling the damage tolerance design for AM parts [63]. Although this study does not provide the overall fatigue properties, the data and the knowledge generated for five contemporary LB-PBF Al alloys built in different orientations can help AM users select a proper Al alloy for their application. Nevertheless, the AM users may need to generate more data for each alloy before using them in specific applications. Fatigue prediction modeling [64] is recommended in future studies for the LB-PBF Al alloys presented here to expedite their adoption to various industries, particularly aerospace.

CRediT authorship contribution statement

P.D. Nezhadfar: Conceptualization, Methodology, Validation, Formal analysis, Data curation, Investigation, Writing – original draft, Visualization. **Spencer Thompson:** Conceptualization, Resources, Validation, Writing – review & editing. **Ankit Saharan:** Conceptualization, Resources, Validation, Writing – review & editing. **Nam Phan:**

Conceptualization, Funding acquisition, Validation, Writing – review & editing. **Nima Shamsaei:** Conceptualization, Methodology, Resources, Formal analysis, Investigation, Writing – review & editing, Supervision, Project administration.

Declaration of Competing Interest

The authors declare that they have no known competing financial interests or personal relationships that could have appeared to influence the work reported in this paper.

Acknowledgment

Partial supports from the U.S. Naval Air Systems Command (NAVAIR) and EOS North America Inc. are acknowledged. This material is also based upon work partially supported by the National Science Foundation (NSF) under grant #1919818.

References

[1] X. Zhang, E. Liang, Metal additive manufacturing in aircraft: current application, opportunities and challenges, IOP Conf. Ser.: Mater. Sci. Eng. 493 (2019), 012032.
[2] J. Gockel, L. Sheridan, B. Koerper, B. Whip, The influence of additive manufacturing processing parameters on surface roughness and fatigue life, Int. J. Fatigue 124 (2019) 380–388.
[3] W.E. Frazier, Metal additive manufacturing: a review, J. Mater. Eng. Perform. 23 (2014) 1917–1928.
[4] S.R. Daniewicz, N. Shamsaei, An introduction to the fatigue and fracture behavior of additive manufactured parts, Int. J. Fatigue 94 (2017) 167.
[5] Y. Murakami, T. Takagi, K. Wada, H. Matsunaga, Essential structure of S-N curve: prediction of fatigue life and fatigue limit of defective materials and nature of scatter, Int. J. Fatigue 146 (2021), 106138.
[6] Z. Wu, S. Wu, J. Bao, W. Qian, S. Karabal, W. Sun, P.J. Withers, The effect of defect population on the anisotropic fatigue resistance of AlSi10Mg alloy fabricated by laser powder bed fusion, Int. J. Fatigue 151 (2021), 106317.
[7] J. Bao, S. Wu, P.J. Withers, Z. Wu, F. Li, Y. Fu, W. Sun, Defect evolution during high temperature tension-tension fatigue of SLM AlSi10Mg alloy by synchrotron tomography, Mater. Sci. Eng.: A 792 (2020), 139809.
[8] J. Bao, Z. Wu, S. Wu, P.J. Withers, F. Li, S. Ahmed, A. Benaarbia, W. Sun, Hot dwell-fatigue behaviour of additively manufactured AlSi10Mg alloy: Relaxation, cyclic softening and fracture mechanisms, Int. J. Fatigue 151 (2021), 106408.
[9] J.W. Pegues, S. Shao, N. Shamsaei, N. Sanaei, A. Fatemi, D.H. Warner, P. Li, N. Phan, Fatigue of additive manufactured Ti-6Al-4V, Part I: the effects of powder feedstock, manufacturing, and post-process conditions on the resulting microstructure and defects, Int. J. Fatigue 132 (2020), 105358.
[10] G. Morettini, S.M.J. Razavi, G. Zucca, Effects of build orientation on fatigue behavior of Ti-6Al-4V as-built specimens produced by direct metal laser sintering, in: Procedia Struct. Integr., Elsevier B.V, 2019, pp. 349–359.
[11] Y.N. Hu, S.C. Wu, P.J. Withers, J. Zhang, H.Y.X. Bao, Y.N. Fu, G.Z. Kang, The effect of manufacturing defects on the fatigue life of selective laser melted Ti-6Al-4V structures, Mater. Des. 192 (2020), 108708.
[12] P. Bajaj, A. Hariharan, A. Kini, P. Kürnsteiner, D. Raabe, E.A. Jägle, Steels in additive manufacturing: a review of their microstructure and properties, Mater. Sci. Eng. A (2019), 138633.
[13] C. Qiu, M. Al Kindi, A.S. Aladawi, I. Al Hatmi, A comprehensive study on microstructure and tensile behaviour of a selectively laser melted stainless steel, Sci. Rep. 8 (2018) 7785.
[14] P.D. Nezhadfar, N. Shamsaei, N. Phan, Enhancing ductility and fatigue strength of additively manufactured metallic materials by preheating the build platform, Fatigue Fract. Eng. Mater. Struct. 44 (2021) 257–270.
[15] D. Deng, R.L. Peng, H. Brodin, J. Moverare, Microstructure and mechanical properties of Inconel 718 produced by selective laser melting: sample orientation dependence and effects of post heat treatments, Mater. Sci. Eng. A 713 (2018) 294–306.
[16] A. Jinoop, C. Paul, K. Bindra, Laser-assisted directed energy deposition of nickel super alloys: a review, Proc. Inst. Mech. Eng. Part L J. Mater. Des. Appl. (2019), 146442071985265.
[17] P.D. Nezhadfar, A.S. Johnson, N. Shamsaei, Fatigue behavior and microstructural evolution of additively manufactured Inconel 718 under cyclic loading at elevated temperature, Int. J. Fatigue 136 (2020), 105598.
[18] J. Zhang, B. Song, Q. Wei, D. Bourell, Y. Shi, A review of selective laser melting of aluminum alloys: processing, microstructure, property and developing trends, J. Mater. Sci. Technol. 35 (2019) 270–284.
[19] P. Rometsch, Q. Jia, K.V. Yang, X. Wu, Aluminum alloys for selective laser melting – towards improved performance, Addit. Manuf. Aerosp. Ind. (2019) 301–325.
[20] N.T. Aboulkhair, N.M. Everitt, I. Maskery, I. Ashcroft, C. Tuck, Selective laser melting of aluminum alloys, MRS Bull. 42 (2017) 311–319.
[21] N.T. Aboulkhair, M. Simonelli, L. Parry, I. Ashcroft, C. Tuck, R. Hague, 3D printing of aluminium alloys: additive manufacturing of aluminium alloys using selective laser melting, Prog. Mater. Sci. 106 (2019), 100578.
[22] J.H. Martin, D. Yahata, J.M. Hundley, J.A. Mayer, T.A. Schaedler, T.M. Pollock, 3D printing of high-strength aluminium alloys, 2017.
[23] M. Tang, P.C. Pistorius, Oxides, porosity and fatigue performance of AlSi10Mg parts produced by selective laser melting, Int. J. Fatigue 94 (2017) 192–201.
[24] S. Bagherifard, N. Beretta, S. Monti, M. Riccio, M. Bandini, M. Guagliano, On the fatigue strength enhancement of additive manufactured AlSi10Mg parts by mechanical and thermal post-processing, Mater. Des. 145 (2018) 28–41.
[25] I. Maskery, R. Aboulkhair, NT, C. Tuck, Wildman, Fatigue performance enhancement of selectively laser melted aluminium alloy by heat treatment, in: Solid Free. Fabr. Symp, 2015.
[26] A. du Plessis, S. Beretta, Killer notches: The effect of as-built surface roughness on fatigue failure in AlSi10Mg produced by laser powder bed fusion, Addit. Manuf. 35 (2020), 101424.
[27] N.E. Uzan, S. Ramati, R. Shneck, N. Frage, O. Yeheskel, On the effect of shot-peening on fatigue resistance of AlSi10Mg specimens fabricated by additive manufacturing using selective laser melting (AM-SLM), Addit. Manuf. 21 (2018) 458–464.
[28] Z.M. Jian, G.A. Qian, D.S. Paolino, A. Tridello, F. Berto, Y.S. Hong, Crack initiation behavior and fatigue performance up to very-high-cycle regime of AlSi10Mg fabricated by selective laser melting with two powder sizes, Int. J. Fatigue 143 (2021), 106013.
[29] J.N. Domfang Ngnekou, Y. Nadot, G. Henaff, J. Nicolai, W.H. Kan, J.M. Cairney, L. Ridosz, Fatigue properties of AlSi10Mg produced by Additive Layer Manufacturing, Int. J. Fatigue 119 (2019) 160–172.
[30] EOS, Material data sheet: EOS AlSi10Mg, 2014.
[31] P. Van Cauwenbergh, G.K. Muralidharan, P. Bigot, L. Thijs, B. Van Hooreweder, K. Vanmeensel, Reducing hydrogen pores and blisters by novel strategies and tailored heat treatments for laser powder bed fusion of AlSi7Mg0.6, Eur. Powder Metall. Assoc. (2019) 1–7.
[32] X. Lesperance, P. Ilie, A. Ince, Very high cycle fatigue characterization of additively manufactured AlSi10Mg and AlSi7Mg aluminium alloys based on ultrasonic fatigue testing, Fatigue Fract. Eng. Mater. Struct. 44 (2021) 876–884.
[33] E. Bassoli, L. Denti, A. Comin, A. Sola, E. Tognoli, Fatigue behavior of as-built L-PBF A357.0 parts, in: Metals (Basel), 8, 2018, p. 634.
[34] EOS, Material Data Sheet EOS Aluminium AlF357 Light Weight & Corrosion resistance, 2019.
[35] APWORKS AIRBUS GmbH, Scalmalloy-state of the art high-strength alloy, 2017.
[36] A.B. Spierings, K. Dawson, K. Kern, F. Palm, K. Wegener, SLM-processed Sc- and Zr-modified Al-Mg alloy: mechanical properties and microstructural effects of heat treatment, Mater. Sci. Eng. A. 701 (2017) 264–273.
[37] M. Awd, J. Tenkamp, M. Hirtler, S. Siddique, M. Bambach, F. Walther, Comparison of microstructure and mechanical properties of Scalmalloy® produced by selective laser melting and laser metal deposition, Materials (Basel) 11 (2017).
[38] M. Muhammad, P.D. Nezhadfar, S. Thompson, A. Saharan, N. Phan, N. Shamsaei, A comparative investigation on the microstructure and mechanical properties of additively manufactured aluminum alloys, Int. J. Fatigue 146 (2021), 106165.
[39] America Makes, AMSC, Standardization Roadmap for Additive Manufacturing - Version 2.0, Am. Makes ANSI Addit, Manuf. Stand. Collab. 2 (2018) 1–203.
[40] N. Shamsaei, A. Yadollahi, L. Bian, S.M. Thompson, An overview of Direct Laser Deposition for additive manufacturing; Part II: mechanical behavior, process parameter optimization and control, Addit. Manuf. 8 (2015) 12–35.
[41] Q. Jia, P. Rometsch, P. Kürnsteiner, Q. Chao, A. Huang, M. Weyland, L. Bourgeois, X. Wu, Selective laser melting of a high strength AlMnSc alloy: Alloy design and strengthening mechanisms, Acta Mater. 171 (2019) 108–118.
[42] EOS, Material data sheet - FlexLine EOS Aluminium AlSi10Mg Material data sheet - FlexLine, 49, 2018: 1–4.
[43] ASTM E606/E606M, Standard Test Method for Strain-Controlled Fatigue Testing, ASTM Stand., 2012.
[44] K. Schmidtke, F. Palm, A. Hawkins, C. Emmelmann, Process and mechanical properties: applicability of a scandium modified Al-alloy for laser additive manufacturing, Phys. Procedia 12 (2011) 369–374.
[45] ASTM WK49229, New Guide for Orientation and Location Dependence Mechanical Properties for Metal Additive Manufacturing, n.d.
[46] A.B. Spierings, K. Dawson, P.J. Uggowitzer, K. Wegener, Influence of SLM scan-speed on microstructure, precipitation of Al 3 Sc particles and mechanical properties in Sc- and Zr-modified Al-Mg alloys, Mater. Des. 140 (2018) 134–143.
[47] J.R. Croteau, S. Griffiths, M.D. Rossell, C. Leinenbach, C. Kenel, V. Jansen, D. N. Seidman, D.C. Dunand, N.Q. Vo, Microstructure and mechanical properties of Al-Mg-Zr alloys processed by selective laser melting, Acta Mater. 153 (2018) 35–44.
[48] S. Kou. Welding Metallurgy, 2nd ed..,, Cambridge University Press, 2020.
[49] M. Mukherjee, Effect of build geometry and orientation on microstructure and properties of additively manufactured 316L stainless steel by laser metal deposition, Materialia 7 (2019), 100359.
[50] M. de, H. van, NLR-Netherlands Aerospace Centre CUSTOMER: European Commission Material Selection and Component Optimization for a Pumped Two-Phase Cooling System Using Additive Manufacturing, 2018. ⟨www.nlr.nl⟩ (accessed 22 June 2021).
[51] S. Begoc, F. Montredon, G. Pommatau, G. Leger, M. Gas, S. Eyrignoux, Additive manufacturing of Scalmalloy® satellite parts, n.d.
[52] S. Defanti, E. Bassoli, Repeatability of the fatigue performance of additively manufactured A357.0 under different thermal treatment conditions, Mater. Sci. Eng.: A 805 (2021), 140594.
[53] A.J. Sterling, B. Torries, N. Shamsaei, S.M. Thompson, D.W. Seely, Fatigue behavior and failure mechanisms of direct laser deposited Ti–6Al–4V, Mater. Sci. Eng. A 655 (2016) 100–112.

[54] K. Solberg, F. Berto, What is going on with fatigue of additively manufactured metals? Mat. Des. amp; Process Comms 1 (2019), e84.
[55] M. Muhammad, P. Frye, J. Simsiriwong, S. Shao, N. Shamsaei, An investigation into the effects of cyclic strain rate on the high cycle and very high cycle fatigue behaviors of wrought and additively manufactured Inconel 718, Int. J. Fatigue 144 (2021), 106038.
[56] Y. Murakami, Metal Fatigue: Effects of Small Defects and Nonmetallic Inclusions, Elsevier, 2002.
[57] R.I. Stephens, A. Fatemi, R.R. Stephens, H.O. Fuchs, Metal Fatigue in Engineering, John Wiley & Sons, 2000.
[58] A. Yadollahi, N. Shamsaei, S.M. Thompson, A. Elwany, L. Bian, Effects of building orientation and heat treatment on fatigue behavior of selective laser melted 17-4 PH stainless steel, Int. J. Fatigue 94 (2017) 218–235.
[59] R. Shrestha, N. Shamsaei, M. Seifi, N. Phan, 1H NMR-based metabolic profiling of cordyceps militaris to correlate the development process and anti-cancer effect, J. Microbiol Biotechnol. 29 (2019) 1212–1220.
[60] A. Soltani-Tehrani, R. Shrestha, N. Phan, M. Seifi, N. Shamsaei, Establishing specimen property to part performance relationships for laser beam powder bed fusion additive manufacturing, Int. J. Fatigue 151 (2021), 106384.
[61] B. Torries, N. Shamsaei, Fatigue behavior and modeling of additively manufactured Ti-6Al-4V including interlayer time interval effects, Jom 69 (2017) 2698–2705.
[62] C. Xie, S. Wu, Y. Yu, H. Zhang, Y. Hu, M. Zhang, G. Wang, Defect-correlated fatigue resistance of additively manufactured Al-Mg4.5Mn alloy with in situ micro-rolling, J. Mater. Process. Technol. 291 (2021), 117039.
[63] U. Zerbst, G. Bruno, J.Y. Buffière, T. Wegener, T. Niendorf, T. Wu, X. Zhang, N. Kashaev, G. Meneghetti, N. Hrabe, M. Madia, T. Werner, K. Hilgenberg, M. Koukolíková, R. Procházka, J. Džugan, B. Möller, S. Beretta, A. Evans, R. Wagener, K. Schnabel, Damage tolerant design of additively manufactured metallic components subjected to cyclic loading: state of the art and challenges, Prog. Mater. Sci. 121 (2021), 100786.
[64] C. Li, S. Wu, J. Zhang, L. Xie, Y. Zhang, Determination of the fatigue P-S-N curves – a critical review and improved backward statistical inference method, Int. J. Fatigue 139 (2020), 105789.